Numerical Simulations of a Gravity Wave Event over CCOPE. Part III: The Role of a Mountain–Plains Solenoid in the Generation of the Second Wave Episode

STEVEN E. KOCH

NOAA/OAR/Forecast Systems Laboratory, Boulder, Colorado

FUQING ZHANG

National Center for Atmospheric Research, Boulder, Colorado

MICHAEL L. KAPLAN, YUH-LANG LIN, RONALD WEGLARZ,* AND C. MICHAEL TREXLER

Department of Marine, Earth and Atmospheric Sciences, North Carolina State University, Raleigh, North Carolina

(Manuscript received 16 February 2000, in final form 15 September 2000)

ABSTRACT

Mesoscale model simulations have been performed of the second episode of gravity waves observed in great detail in previous studies on 11–12 July 1981 during the Cooperative Convective Precipitation Experiment. The dominant wave simulated by the model was mechanically forced by the strong updraft associated with a mountain–plains solenoid (MPS). As this updraft impinged upon a stratified shear layer above the deep, well-mixed boundary layer that developed due to strong sensible heating over the Absaroka Mountains, the gravity wave was created. This wave rapidly weakened as it propagated eastward. However, explosive convection developed directly over the remnant gravity wave as an eastward-propagating density current produced by a rainband generated within the MPS leeside convergence zone merged with a westward-propagating density current in eastern Montana. The greatly strengthened cool pool resulting from this new convection then generated a bore wave that appeared to be continuous with the movement of the incipient gravity wave as it propagated across Montana and the Dakotas.

The nonlinear balance equation and Rossby number were computed to explore the role of geostrophic adjustment in the forecast gravity wave generation, as suggested in previous studies of this wave event. These fields did indicate flow imbalance, but this was merely the manifestation of the MPS-forced gravity wave. Thus, the imbalance indicator fields provided no lead time for predicting wave occurrence.

Several sensitivity tests were performed to study the role of diabatic processes and topography in the initiation of the flow imbalance and the propagating gravity waves. When diabatic effects owing to precipitation were prevented, a strong gravity wave still was generated in the upper troposphere within the region of imbalance over the mountains. However, it did not have a significant impact because moist convection was necessary to maintain wave energy in the absence of an efficient wave duct. No gravity waves were present in either a simulation that disallowed surface sensible heating, or the ''flat terrain'' simulation, because the requisite MPS forcing could not occur.

This study highlights difficulties encountered in attempting to model the generation of observed gravity waves over complex terrain in the presence of strong diabatic effects. The complex interactions that occurred between the sensible heating over complex terrain, the incipient gravity wave, and convection highlight the need for much more detailed observations between wave generation regions over mountains and the plains downstream of such regions.

1. Introduction

Our knowledge of gravity waves and the processes that produce organized convection over and downwind of complex terrain remains incomplete. Most of what is generally known about airflow over orography is related to the generation of lee waves, mountain waves, downslope winds, and other orographically fixed phenomena from idealized numerical experiments that emphasize the final steady-state solution. The present study is concerned with propagating hydrostatic gravity waves generated near mountains with widths of 100–500 km, for which buoyancy and Coriolis forces must both be considered. Inertia–gravity waves become increasingly important as the Rossby number increases toward, and

* Current affiliation: Department of Physics, Astronomy, Meteorology, Western Connecticut State University, Danbury, Connecticut.

Corresponding author address: Dr. Steven E. Koch, NOAA Forecast Systems Laboratory, R/FS1, 325 Broadway, Boulder, CO 80303. E-mail: koch@fsl.noaa.gov

then exceeds, unity. Their phase lines tilt upstream, just as in the case of smaller-scale mountains, with the disturbance energy propagating upward and downstream relative to the mountains (Smith 1979).

The situation becomes considerably more complex when sensible heating over elevated terrain is considered. It is well established from linear theory that stationary mountain waves are weakened by sensible heating as high Froude number air flows over a two-dimensional ridge, yet propagating gravity waves are generated in response to the heating (Raymond 1972; Lin 1994). Furthermore, the vertical velocity field is sensitive to the Richardson number and the depth of the heated layer when a wave critical level is present (Lin 1987). Gravity waves generated in a stably stratified shear layer by diabatic forcing in the absence of terrain show phase lines tilting upstream against the shear (Clark et al. 1986; Fovell et al. 1992; Lott 1997), but gravity waves generated by diabatic heating over terrain have not been studied extensively.

Banta (1984) created a conceptual model to explain the development of a thermally forced circulation in a mountain valley generated by solar heating. Just before sunrise, a very stable layer is found adjacent to the surface due to nighttime cooling. As surface heating begins after sunrise, it erodes the inversion layer from below. The inversion breaks first near the mountaintop, allowing westerly momentum from above the inversion to be mixed downward to the surface and create downslope winds on the lee slope. At the same time, the warming of the sloping terrain relative to the free atmosphere at the same height lowers the pressure, creating a horizontal pressure gradient forcing air beneath the inversion to rise up the mountain. A leeside convergence zone (LCZ) forms where the upslope flow converges with the downslope flow (Banta 1990; May and Wilczak 1993). The mountain–plains solenoid (MPS) is a broader (>100 km scale) version of this diurnally oscillating system (Tyson and Preston-Whyte 1972). The daytime MPS over the Rocky Mountains is characterized by low-level upslope easterly flow, strong upward motion at the LCZ just downwind (to the east) of the mountain ridge, and an oppositely directed return current in the midlevels (Toth and Johnson 1985).

Idealized, two-dimensional numerical experiments have been performed of the MPS over the Front Range of the Rocky Mountains in Colorado. Bossert and Cotton (1994) studied the effects of wind and stratification on the MPS circulation. Wolyn and McKee (1994) developed a useful conceptual model of the daytime MPS from their model experiments. A katabatic jetlike flow down the eastern side of the mountain is the most pronounced feature of the wind field in the sunrise state (Fig. 1a). A ''stable core'' is created as this nocturnal jet decelerates and lifts the stable air over the eastern plains. This katabatic flow weakens as it is affected by the surface heating, and is replaced by a mesoscale solenoid circulation 3–4 h after sunrise (Fig. 1b). Rising air within the LCZ creates a ''cold core'' as the updraft impinges upon the statically stable air above the deep, well-mixed boundary layer over the mountain. A horizontal pressure gradient is produced since the pressure along an isentropic surface in the cold core is much higher than that to its east. As a result, the basic westerly flow is accelerated in the return current (the ''wind speed maximum''). The final phase (Fig. 1c) is characterized by the eastward migration of the solenoid, provided that

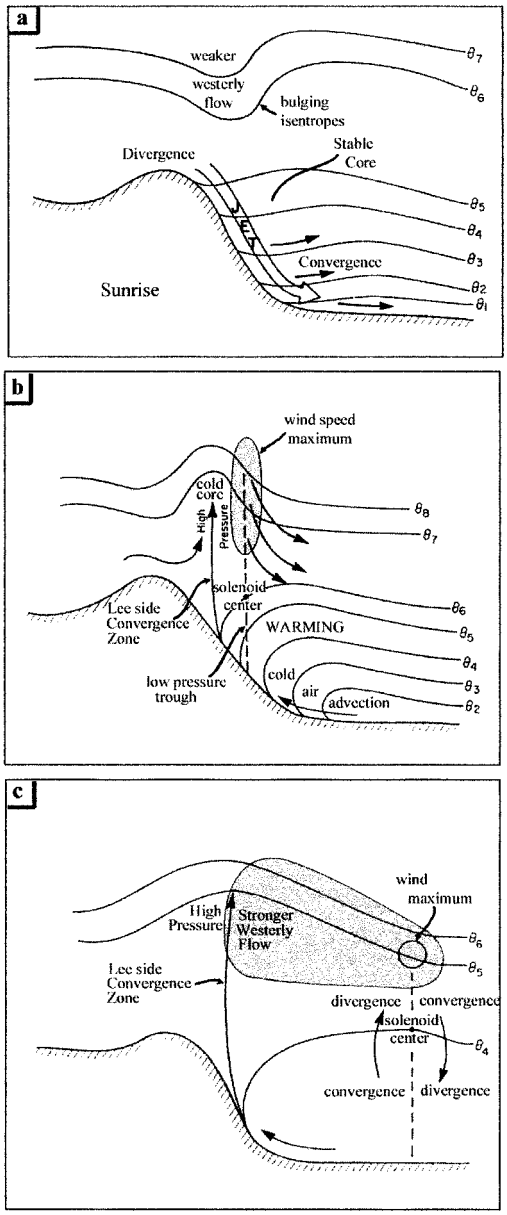

FIG. 1. Conceptual model of the daytime evolution of the MPS circulation east of a 2-km-high and 60-km-wide mountain under conditions of clear skies, steady-state synoptic-scale conditions, and light ambient winds with a westerly component of ~5 m s^{-1}. (a) Sunrise state, (b) developing MPS, and (c) migrating MPS [after Wolyn and McKee (1994)].

sensible heating is strong enough; note, though, that the LCZ remains anchored back over the lee slopes.

Two-dimensional moist model simulations by Tripoli and Cotton (1989a,b) suggest that gravity waves may interact with the MPS circulation to produce and alter strong convection. Their results show that storms forming above the LCZ grew as they propagated eastward into a stationary wave updraft region located about 60 km downwind of the peak. As the storms left the LCZ behind in their continued propagation downslope, they weakened and simultaneously generated a deep gravity wave 150–200 km in horizontal wavelength. Although this gravity wave failed to trigger substantial convection in their model, other trapped gravity waves that were generated later as radiative cooling occurred above the cloud top triggered new convective cells away from the main convective core. These model results suggest that the MPS can be responsible for the generation of ''secondary convection'' (Banta 1990) well to the east of the original forcing, which can even develop into a mesoscale convective complex (MCC). Maddox et al. (1981) discuss how MCCs bring a large percentage of the summer rainfall to the Great Plains states and that the genesis of nearly half of all MCCs occurs over the eastern slopes of the Rocky Mountains.

Little is presently understood about the interaction of the MPS with the synoptic-scale flow in situations of moderate to strong shear, and the possibility that this may lead to the generation of propagating gravity waves in the absence of convection. Kaplan et al. (1997) performed dry three-dimensional numerical model simulations of a gravity wave event observed on 11–12 July 1981 in Montana and the Dakotas region during the Cooperative Convective Precipitation Experiment (CCOPE). They suggested that strong vertical wind shear associated with a midlevel jet was important in the generation of the second of two gravity wave episodes in this event. Koch and Golus (1988), Koch et al. (1988), and Koch et al. (1993) observed the waves and their vertical structure in detail with mesoscale surface observations and multiple Doppler radar analysis and pressure retrievals. The observed waves, which displayed a dominant wavelength of 135 km, were backtracked to an apparent generation region over the Absaroka Mountains in southwestern Montana or northwestern Wyoming (Fig. 2b). The waves spawned severe thunderstorms over the CCOPE region culminating in the generation of an MCC after 0200 UTC 12 July.

Koch and Dorian (1988) argued that geostrophic adjustment and shear instability were the two most likely wave source mechanisms in the CCOPE wave event. Koch et al. (1993) showed from linear stability analysis that the waves could efficiently extract energy from the mean flow near several closely spaced critical levels in the 4.0–6.5-km layer and that the waves were ducted at low levels. The implied lack of wave tilt below ~3 km was confirmed with multiple Doppler radar pressure retrievals performed at the beginning of the second wave episode. The basis for the geostrophic adjustment suggestion was the diagnosis of unbalanced flow (e.g., large Rossby number) over the wave generation region. However, their use of primarily synoptic-scale rawinsonde data meant that they could not assess the role of any gravity wave generation mechanism operating on scales unresolved by the rawinsonde network, including topography and convective forcing upstream of the CCOPE network. The model simulations performed by Kaplan et al. (1997) failed to simulate the observed propagating gravity waves. Zhang and Koch (2000) successfully simulated the *first* observed wave episode, which was characterized by weak shower activity. Their study revealed that the generation of those gravity waves was due largely to a westward-propagating density current on the eastern mountain slopes rather than geostrophic adjustment. Hence, the actual generation mechanism for wave episode II remains uncertain.

The present study seeks to employ a sophisticated mesoscale model to understand the actual gravity wave generation mechanism(s) operating during wave episode II. Diagnostic analysis of flow imbalance is performed upon the mesoscale model forecast fields to more fully evaluate the role of geostrophic adjustment in generating the waves. Numerical model configurations and experimental design are presented in section 2. The control simulation is compared to the observations of the MPS and the gravity waves in section 3, where the wave generation mechanisms are also discussed. The diagnostic analysis of flow imbalance is performed in section 4. Sensitivity tests with respect to topography and diabatic heating are reported upon in section 5. Shear instability and wave ducting analyses appear in section 6, followed by the conclusions.

2. Numerical model and experimental design

Two models were employed in this study. The numerical model primarily used is version 2 of the nonhydrostatic Pennsylvania State University–National Center for Atmospheric Research (PSU–NCAR) fifth-generation Mesoscale Model (MM5) (Dudhia 1993; Grell et al. 1995). These simulations were performed using a horizontal grid resolution of 16 km and 30 vertical levels. Rather than initializing the simulations at 0000 UTC 11 July 1981 as done by Kaplan et al. (1997) and Zhang and Koch (2000), MM5 was initialized at 1200 UTC 11 July 1981 from a limited fine mesh model analysis reanalyzed with synoptic observations. The model domain and terrain resolution were set equal to those used in those earlier studies, as shown in Fig. 2a. The actual complex topography in and around the wave generation region is shown in Fig. 2b. No grid nesting was applied. The Kain–Fritsch convective parameterization scheme, the Blackadar planetary boundary layer scheme, and an upper radiative boundary condition were used. A 13-category lookup table determined soil properties in the MM5 model. Soil moisture availability var-

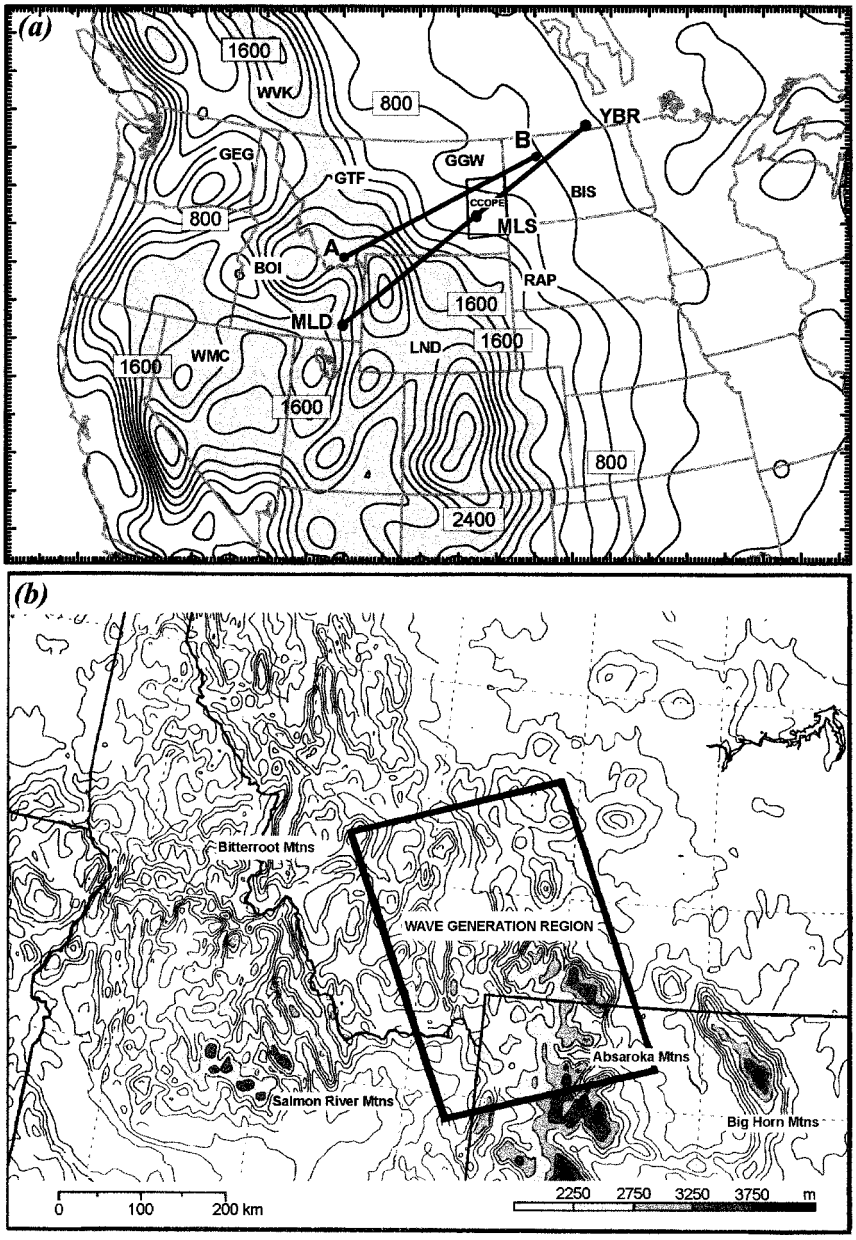

FIG. 2. (a) The model domain and the smoothed terrain data (contour interval 200 m) used for the MM5 simulation. Elevation higher than 1400 m is shaded to highlight the Rocky Mountain barrier. The thick lines A–B and MLD–MLS–YBR depict the location of the cross sections for the control simulation and the idealized model. (b) Actual terrain in the vicinity of the wave generation region in southwestern Montana and northwestern Wyoming [after Koch and Dorian (1988)]. Also shown are the CCOPE mesonetwork [small rectangle in (a)] and nearby rawinsondes.

ied from 30% over the agricultural regions of the Dakotas and the coniferous-forested mountainous regions in western Montana and Idaho to 15% over the range grassland areas of eastern Montana. Analysis of the observations created the lateral boundary conditions in conjunction with a flow relaxation scheme. The model was run for 24 h following a simple static initialization; in fact, a simulation with 12-h preforecast ''nudging'' failed to improve the forecast of the gravity waves.

Results from three sensitivity tests also will be discussed. A summary of the MM5 simulations is shown in Table 1. One of the experiments is a ''fake dry'' simulation similar to that in Kaplan et al. (1997) except that it was begun at 1200 UTC 11 July 1981. Another

TABLE 1. Summary of MM5 numerical experiments.

Expt	Moisture schemes	Description	Purpose
Control	Explicit + Kain–Fritsch	Full physics	Basis for comparison with other more simplified simulations
Fake dry	None	No latent heating or cooling produced by precipitation; sensible heating allowed	Examine effect of precipitation physics on flow imbalance and gravity waves
Adiabatic	None	No heating/cooling due to precipitation; no latent and sensible heat fluxes	Examine influence of sensible heating over complex terrain on flow imbalance and gravity waves
Flat terrain	Explicit + Kain–Fritsch	Terrain heights set to 1.5 km	Examine effect of complex topography on flow imbalance and gravity waves

simulation is a totally ''adiabatic'' version of the control experiment. The ''flat terrain'' experiment uses the average height of 1500 m uniformly across the entire domain. These experiments are designed to examine the influence of the topographic and diabatic processes on the generation of the flow imbalance and gravity waves. In particular, we were interested in isolating basic mountain flow regimes in the presence of varying surface diabatic forcing and moist convection influences.

The second model used in this study is version 4.2.4 of the two-dimensional Advanced Regional Prediction System (ARPS) model (Xue et al. 1995), a nonhydrostatic model with compressible dynamics. The model simulations employed 60 levels on a stretched vertical grid to 20 km, a Rayleigh damping (sponge) layer above 12 km, a horizontal domain 1200 km in length with grid spacing of 5 km, and radiative lateral boundary conditions. A 1.5-order turbulent kinetic energy local closure scheme (Moeng and Wyngaard 1988) was chosen for the boundary layer after tests performed with other schemes produced less satisfactory results. Surface fluxes were calculated from the stability-dependent surface drag coefficient and predicted surface temperature. Special code was developed to import the terrain used in our MM5 simulations to the ARPS grid, and then to interpolate these data to the MLD-to-YBR cross section (locations shown in Fig. 2a). Likewise, the profiles of wind and temperature from the MM5 simulation were used to initialize the ARPS model at 1200 UTC (approximately 1 h before sunrise). In particular, the forecast sounding for Miles City (MLS in Fig. 2a) was used for initializing ARPS. Full moist-physics, fake-dry, and adiabatic simulations were all performed with the ARPS model. Only the fake-dry results are shown herein, because our chief aim in using this idealized model is to help understand the underlying physics governing the generation of gravity waves when a mountain–plains solenoid circulation is well developed.

3. Simulation of the mountain–plains solenoid and gravity waves

The results from the control simulation pertaining to the MPS are first compared to the rawinsonde observations. The gravity waves detected from the mesoanalyses are then related to those simulated. Last, the idealized ARPS model experiments are presented to aid in the understanding of the basic wave forcing mechanisms.

a. Mountain–plains solenoid

Changes from 1200 UTC 11 July to 0000 UTC 12 July 1981 in fields of geopotential heights at 850 and 600 hPa, temperatures at 850 hPa, and the thickness of the 850–600 hPa layer are displayed in Fig. 3. These 12-hourly change fields forecast by the MM5 control simulation clearly show differential sensible heating and the development of a pronounced MPS over the Rocky Mountains. Heights at 850 hPa generally fell by 10–25 m over the mountainous areas, notably in southwestern Montana and eastern Idaho, and increased by a similar amount over the plains to the east. This field is strikingly similar to the 850-hPa temperature change field, which indicates strong warming of 10°–14°C over the mountains and cooling over southeastern Montana. Height change patterns at 600 hPa are generally reversed from those at 850 hPa, with strong height rises of 40–60 m over the mountains and weaker height falls over southeastern Montana and Wyoming. The combined effect of these height changes in the lower and middle troposphere hydrostatically produces the thickness change field shown in Fig. 3d, which consists of a simple dipole pattern of rises over the mountains (particularly over western Montana) and falls over eastern Montana.

These patterns are generally consistent with the observations, as well. The rawinsonde data were subjected to a Barnes objective analysis scheme (Koch et al. 1983). Stations used in this analysis are shown in Fig. 2a. Refer to Koch and Dorian (1988) for details of the objective analysis. The resulting analysis of thickness changes (Fig. 4d) shows a dipole pattern similar to that forecast by MM5. Although this analysis contains much less detail because of the coarse resolution of the rawinsonde data (average data spacing of 384 km), still the gradient of height changes in both the model and the observations (the vectors in Figs. 3 and 4) clearly shows a reversal from one directed toward the mountains at low levels to one directed away from the mountains aloft.

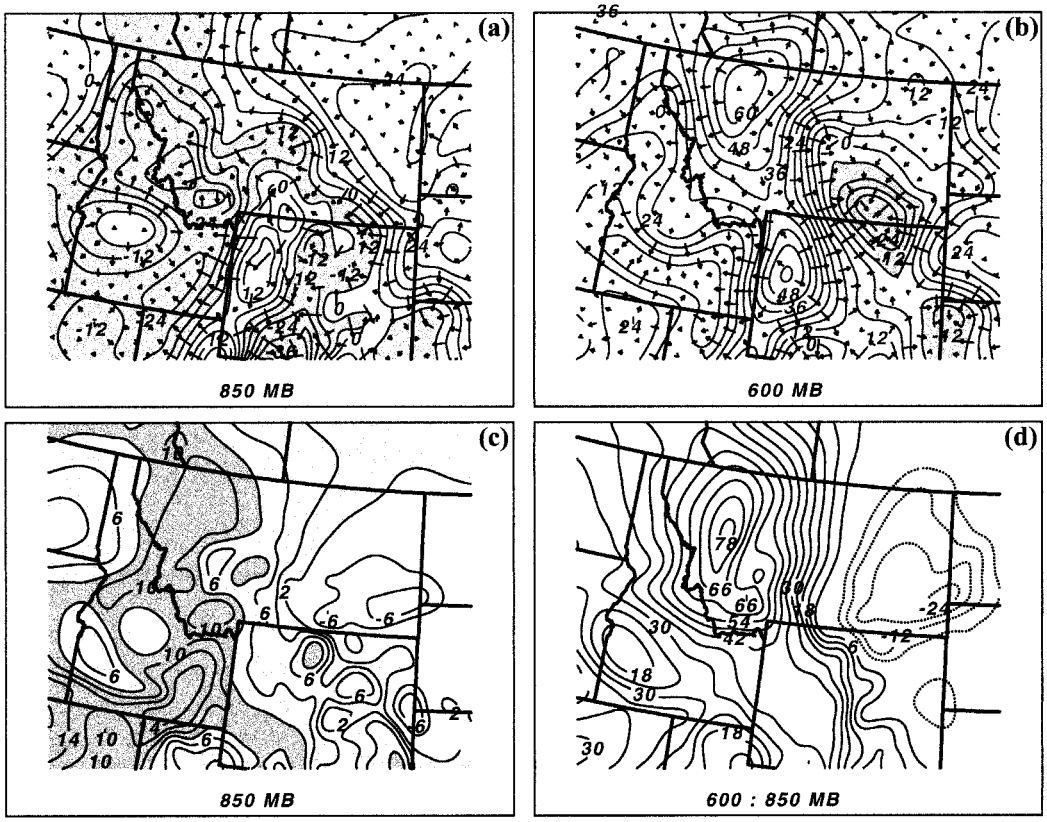

FIG. 3. Forecast fields from MM5 control simulation showing 12-hourly changes (from 1200 UTC 11 Jul to 0000 UTC 12 Jul 1981) of (a) geopotential heights at 850 hPa (6-m contours, height falls are shaded) and gradient of the height change field (vectors), (b) as in (a) except at 600 hPa, (c) temperature at 850 hPa (2°C intervals, zero line omitted, warming indicated by shading), and (d) thickness in the 600–850-hPa layer (6-m contours, rises solid, falls dotted).

Confirmation that sensible heating was the main cause for these change fields is found upon comparing the 12-hourly change fields from the control simulation to those predicted by the adiabatic MM5 run. Very little warming occurs over the mountainous regions in the adiabatic simulation (Fig. 5a) relative to that in the control run. Thickness rises over the mountainous regions are also much less pronounced in the adiabatic run (Fig. 5b) because of the lack of diabatic effects related to elevated sensible heating (though fields over the plains area are similar). Finally, note that analyzed thickness changes *at the location of individual rawinsonde stations* (Fig. 5b) (such as Boise (BOI) and Lander (LND) in Fig. 2a) compare better to those simulated by the control run (Fig. 3d) than to those in the adiabatic simulation (Fig. 5b).

This pattern of low-level height falls and upper-level height rises, and the associated thickness increases, over the mountains during the daytime creates pressure gradient forcing for a pronounced MPS circulation system (Banta 1984; Wolyn and McKee 1994). Hourly cross sections were constructed along the prevailing southwesterly flow and perpendicular to the Absaroka Mountains from Malda, Idaho, to Miles City, Montana (Fig. 2a). A set of cross sections from the control simulation valid at 2000 UTC (Fig. 6) shows all the features associated with a classical MPS circulation system (cf. Fig. 1). Notice in Fig. 6a the presence of upslope flow at low levels from the northeast and the return flow evidenced by the ''wind speed maximum'' in the 400–600-hPa layer just downwind (to the right) of the mountaintop (the wind speed maximum developed at 1800 UTC). This circulation is forced by the pressure gradient produced by the low-level height falls due to the sensible heating and height rises at higher levels associated with the cold core (Fig. 6c). Sensible heating has produced a deep, well-mixed boundary layer over the highest terrain. A strong updraft is located 40 km to the east of the mountaintop above the zone of convergence over the lee slopes (the LCZ). The entire MPS circulation system is quite evident in Fig. 6d.

A unique and unexpected feature that was not discussed by Wolyn and McKee (1994) or others is also present in these cross sections. Vertically propagating gravity waves are evident downwind of the mountaintop (Figs. 6b and 6c). These waves are of considerable interest to the current study. They were not present in

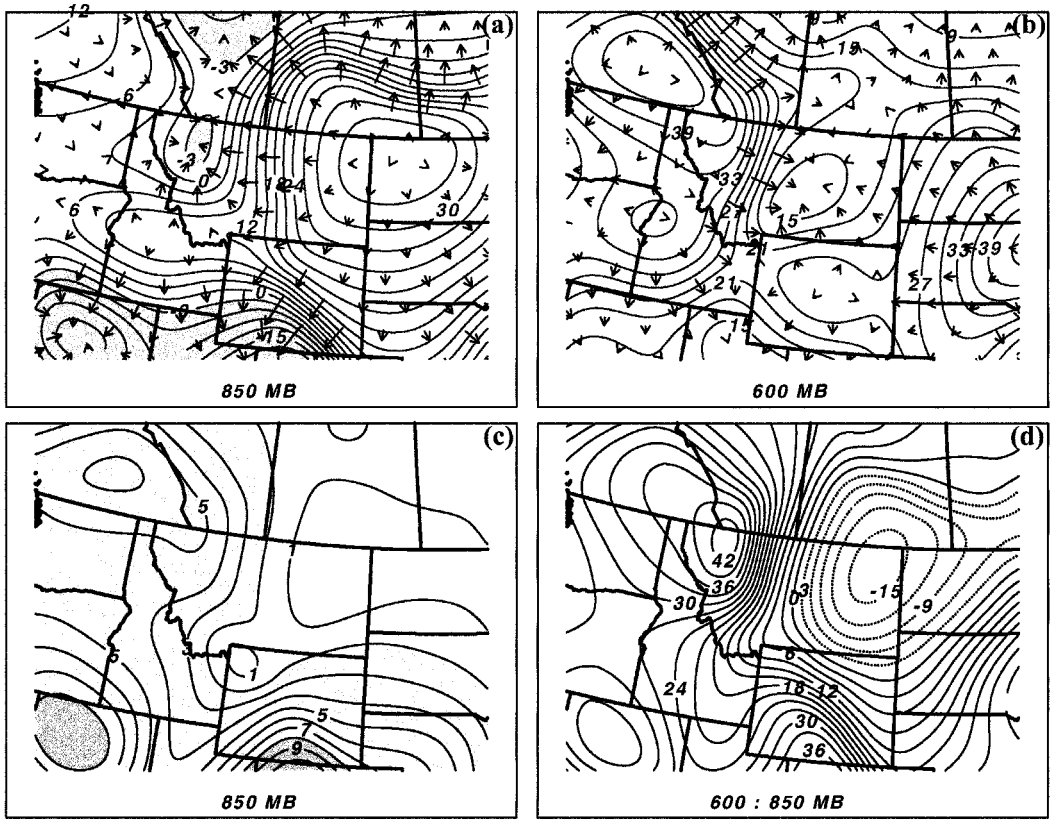

FIG. 4. As in Fig. 3 except resulting from objective analysis of the rawinsonde data. Station locations are shown in Fig. 2.

either the adiabatic simulation, which disallowed surface sensible heating, or the flat-terrain simulation. Cross sections from the adiabatic simulation valid at 2000 UTC (Fig. 7) do not show any evidence of the waves, differential sensible heating, or any of the features associated with the MPS circulation (the LCZ, the return flow, etc.). The single updraft–downdraft couplet over the mountain is a gravity wave forced by a westward-propagating density current [similar to one discussed by Jin et al. (1996)] and dies out soon thereafter as the current approaches the mountaintop. This highly unrealistic feature of the adiabatic simulation occurs because, in the absence of sensible heating, the easterly low-level flow present initially in the model simply advects the cool air westward. In summary, the gravity waves simulated by MM5 require an MPS circulation associated with sensible heating over elevated terrain.

b. Gravity waves

The gravity waves present in the control run are investigated in detail here. In order to facilitate direct comparisons between the model simulations of gravity waves and those observed, subjective surface mesoanalyses were constructed. Outflow boundaries were determined by analyzing the surface observations on an hourly basis, and synthesizing these analyses with the satellite and radar imagery and detailed mesoscale observations over the CCOPE mesonetwork (Fig. 2a), as discussed further in Koch et al. (1988). The mesoanalyses are displayed every 3 h from 1500 UTC 11 July to 0600 UTC 12 July in Fig. 8. The synoptic-scale pattern consisted of a stationary front over Wyoming and South Dakota, a low pressure system over northwestern Nebraska, and an inverted trough extending from this cyclone across eastern Montana (including the CCOPE region). This basic surface picture remained essentially unchanged throughout this entire period except that the inverted trough became lost in a mire of thunderstorm outflow boundaries that marched across the region.

Gravity waves 1 and 2 compose part of the first episode of the gravity waves. Bands of weak showers were associated with each wave crest, which is why a weak outflow boundary surrounds the southern part of each wave in Fig. 8. Significant changes occur by 2100 UTC as warm air surges northward in response to a cyclonic circulation that has developed in southwestern Montana because of the intense sensible heating over the mountains. Two new gravity waves (3 and 4) are seen propagating away from this region along an outflow boundary left behind by the rain-cooled air produced earlier by waves 1 and 2, which have by this time advanced

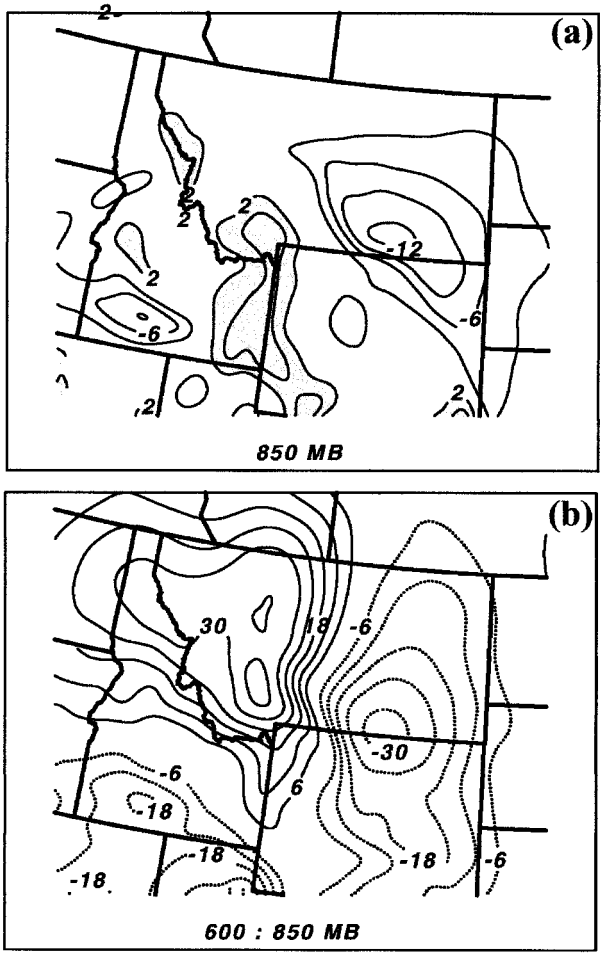

FIG. 5. As in Figs. 3c,d, except that the 12-hourly change fields are from MM5 adiabatic simulation of (a) temperature and (b) thickness in the 600–850-hPa layer.

into central North Dakota. Moist convection does not attend wave 3 until 0300 UTC; however, wave 4 was convective and displayed a moderately strong pressure signal from its very beginning (Fig. 9). As wave 4 passes over the stationary outflow boundary draped across the northwestern corner of the CCOPE mesonetwork (Fig. 8d), where it encounters strong potential instability and low convective inhibition (Koch and Dorian 1988), thunderstorms develop explosively. Strong convection is triggered repeatedly thereafter as gravity waves 4, 5, and 6 pass over the CCOPE mesonet. These severe thunderstorms quickly develop into a massive mesoscale convective complex. Notice in the isochrone analysis (Fig. 9) that the waves displayed a consistent change in propagation characteristics from northeasterly movement to southeasterly as strong convection developed along the wave crests. This change in behavior arose as new convective cells formed along each gust front (Koch et al. 1988).

The control simulation forecasts of mean sea level pressure field are displayed in Fig. 10 every 3 h at the same times shown in Fig. 8. Similar to the observations, a lee cyclone is forecast in extreme northwestern Nebraska and a stationary front extends to the west and east from this cyclone. Also in good agreement is the north–south-oriented inverted trough in extreme eastern Wyoming and western North Dakota at 1500 UTC (though MM5 was not able to develop so early in the forecast a rain-cooled outflow boundary in North Dakota like that seen in Fig. 8b). The lee cyclone and the stationary front show little movement over the next 21 h except over northwestern Wyoming, where a sudden surge northward of the front and cyclogenesis occurs in response to intense elevated terrain heating, just as in the observations.

Three gravity waves (A, B, and C in Fig. 10) were also produced during the 24-h simulation. All of these waves were associated with rain-cooled outflow regions. Existence of all outflow regions (or ''cool pools'') was confirmed from the forecast potential temperature fields (not shown). Hourly isochrones of the three waves are depicted in Fig. 11, for comparison with the observed wave isochrones (Fig. 9). Next, we describe the morphology of each gravity wave.

1) GRAVITY WAVE A

Wave A first appeared in the forecast mean sea level pressure fields in central Montana only a couple of hours after model initialization and subsequently propagated eastward with a phase speed of 16 m s^{-1}. Although an arc-shaped outflow boundary surrounds wave crest A at 1500 UTC (Fig. 10a), very little precipitation was ever associated with wave A and even this ended as the wave advanced into the Dakotas. Evidence that this disturbance was indeed a gravity wave exists in the fact that there was a quadrature phasing between the vertical motions and the isentropes (discussed later with reference to Fig. 13b). Wave A shares characteristics somewhat similar to those of observed wave 1 and/or 2 (Fig. 8). However, given the fact that this disturbance was generated so early in the model forecast, its realism may be questioned because of possible problems associated with initial imbalance remaining after the static model initialization. In addition, it was difficult to distinguish gravity wave characteristics along the southern portion of this disturbance once moist convection developed along the wave. Thus, wave A is not the primary focus of our study.

2) GRAVITY WAVE B

Simulated wave B first appeared in the pressure field soon after 2000 UTC about 200 km to the west of the CCOPE mesonetwork. This wave developed explosively within a saturated, convectively unstable layer in the midtroposphere and had the structure of a wave-CISK (conditional instability of the second kind) mode (Ray-

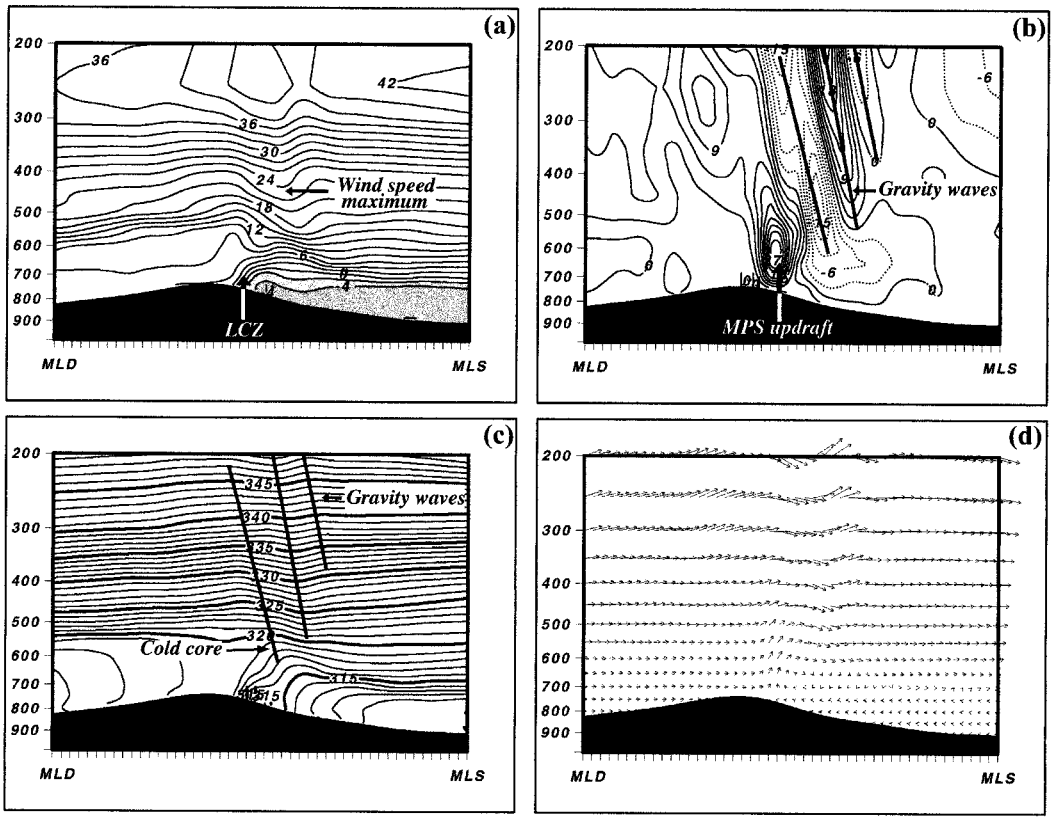

FIG. 6. Cross sections from Malda, ID, to Miles City, MT (line MLD–MLS in Fig. 2a) from control simulation valid at 2000 UTC 11 Jul 1981 of (a) horizontal wind in the plane of the cross section [m s^{-1}, negative (northeasterly) flow shaded], (b) vertical motion [cm s^{-1}, upward (downward) motions depicted by solid (dotted) lines], (c) potential temperature (solid lines, 1-K isentropes), and (d) two-dimensional wind vectors (vertical component is enhanced over the horizontal component by a factor of 3). Total length of cross section is 730 km (ordinate is hPa). Lines in (c) denote phase lines for upward propagating gravity waves.

mond 1975, 1984) throughout its lifetime as it was always accompanied by strong convective activity. Plots of the model cross section fields made only 6 min apart show this rapid evolution (Fig. 12). Wave B became detectable as strong diabatic heating from convection enhanced the upward motion from the initial value of only 3 cm s^{-1} at 2003 UTC to 12 cm s^{-1} at 2009 UTC, and eventually reaching 60 cm s^{-1} by 2100 UTC. Cold outflow produced by the intense convection attending this gravity wave created a strong gust front on its eastern edge, similar to that of a squall line, while a secondary reinforcement of this cool pool developed just to the west of the CCOPE mesonetwork by 0000 UTC 12 July (Fig. 10d). This wave propagated at the same speed as the newly triggered convection and displayed an in-phase relationship between upward motion and diabatic heating (implied by the vertical spreading of isentropes in Fig. 13c). Both of these characteristics are consistent with wave-CISK concepts.

3) GRAVITY WAVE C

The MM5 control run fields become dominated by convection after wave B develops. In addition to wave B's cold outflow and the reinforcing cool pool to its west at 0000 UTC 12 July, another outflow boundary resulting from precipitation forced by the LCZ begins to slide down the eastern slopes of the Absaroka Mountains (Fig. 10d). The two outflow boundaries collide soon thereafter, triggering even stronger convection associated with wave C (Figs. 10e,f). These complex interactions are discussed in greater detail below.

The origin of wave C is best understood with the help of vertical cross sections constructed along line A–B (Fig. 10a). During midmorning (Fig. 13a), the flow was primarily southwesterly and unperturbed, with the exception of rising motion associated with wave A (which is barely seen here since the location of this particular cross section lies just to its north). The low-level stable layer over the mountain slopes disappears entirely by 1800 UTC due to strong surface sensible heating, and an upslope flow forms in association with the developing MPS (Fig. 13b). The LCZ is ~50 km to the east of the mountaintop, while the sinking branch of the MPS is observed 600 km to its east. This represents a broader circulation than that modeled by Wolyn and McKee (1994), a fact explained by the gentler mountain slope

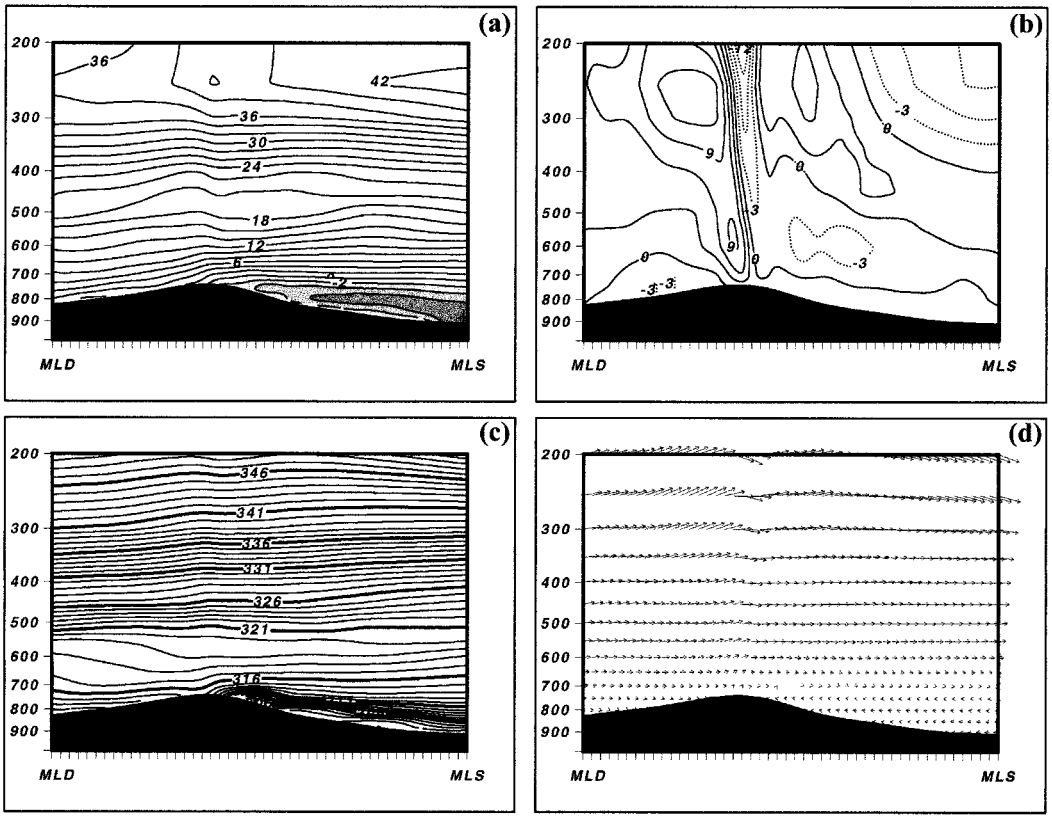

FIG. 7. As in Fig. 6 except from adiabatic simulation.

used in the present simulation. The scale of the upbranch of the circulation is approximately that of the length scale of the sensible heating (half the mountain width), whereas the downbranch has a generally larger scale than the upbranch because it is a compensating return flow. In fact, the ~600 km scale of the MPS is consistent with the scale of differential heating and thickness changes (Figs. 3 and 4).

Wave C is just becoming apparent as part of a vertically propagating gravity wave train above the mountaintop at 1800 UTC. The situation becomes much more complex after this time. First, a strong cool pool is generated by the explosive convection attending wave B by 2100 UTC (Fig. 13c), as mentioned above. The original LCZ can no longer be discerned as a cool pool produced by precipitation that has begun to appear within a developing rainband replaces it near the surface. This cool pool slides down the mountain, and soon thereafter, it collides with the other cool pool left behind by wave B. Vigorous convection is generated as these two outflow boundaries collide directly beneath weak wave C.

Complex interactions between the propagating cool pools (or density currents) and wave C are understood more clearly with the help of the greater detail afforded by Fig. 14, which was constructed from analyses performed upon 15-min model output fields. The density currents are shaded in blue and the updrafts along the outflow boundaries are numbered as $O_1, \ldots, O_4$. Updraft O_1 was generated by the westward-propagating cool pool resulting from wave B, while O_2 and O_3 are the outflow boundaries surrounding the cool pool produced by the LCZ rainband. Updraft O_2 accelerated eastward from 5.6 m s^{-1} at 2200 UTC to 11.1 m s^{-1} by 0100 UTC as the associated density current accelerated down the mountainside under the force of gravity. Counterpropagating outflow boundaries O_1 and O_2 collided soon after 0000 UTC, resulting in a strong updraft O_4 right beneath dissipating wave C (Figs. 14d,f). The mutual reinforcement between O_4 and wave C triggered strong convection, which produced an even stronger cool pool, whereas the original cool pool from wave B disintegrated. Wave C was thereby reinvigorated and subsequently evolved into a bore wave. A bore produces a sustained elevation of the inversion surface accompanied by a surface pressure rise hydrostatically related to the cooling in the column, though no cooling occurs at the surface. Examples of observed and simulated bores can be found in Smith (1988), Haase and Smith (1989), Koch et al. (1991), Karyampudi et al. (1995), Jin et al. (1996), and Locatelli et al. (1998). The bore propagated eastward at a speed of 14.0 m s^{-1}, which is much faster than its preconvective propagation speed (5 m s^{-1}), though only in fair agreement with the observed wave phase speed (18.9 m s^{-1}). Since the observed es-

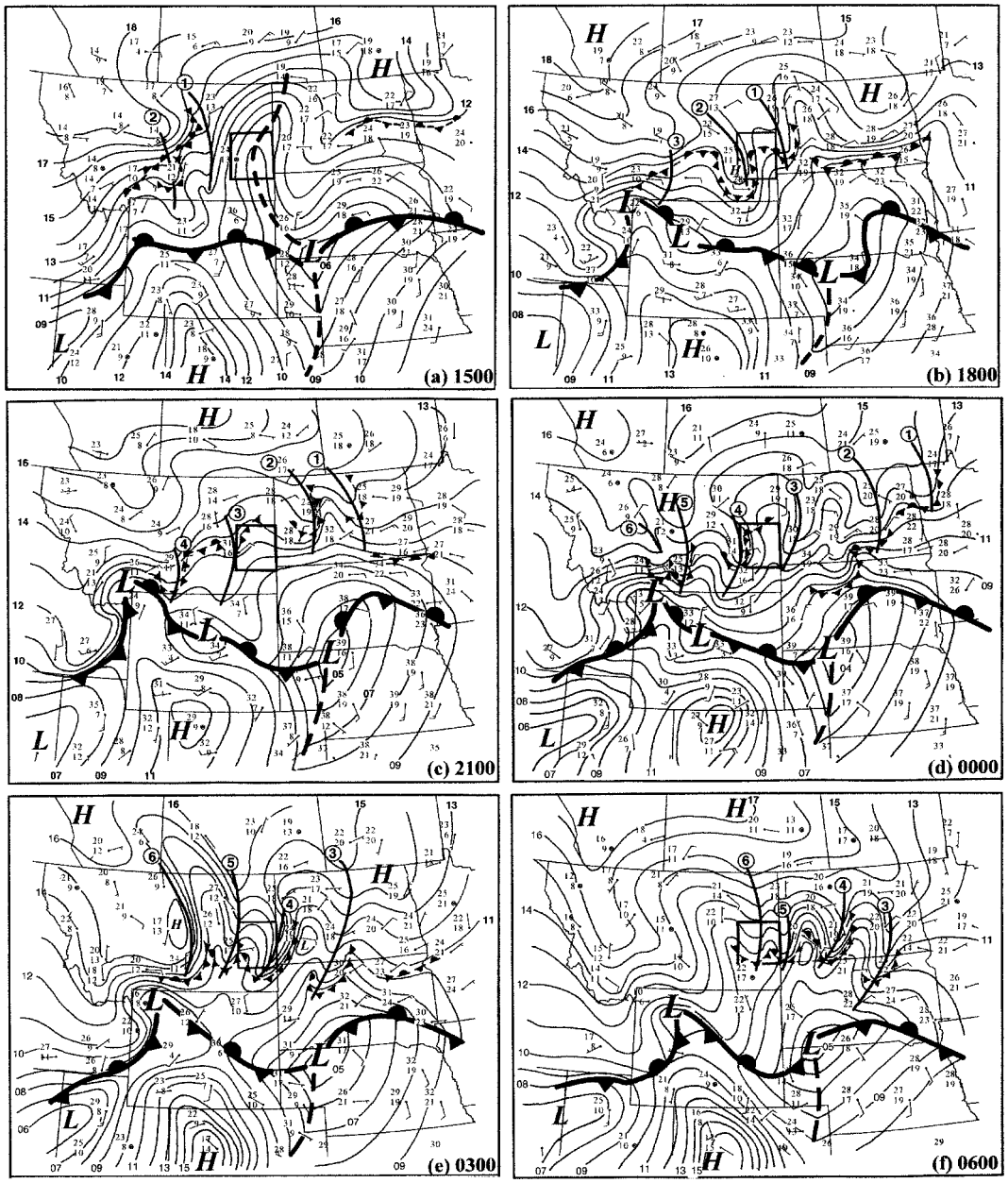

FIG. 8. Subjective surface analyses at (a) 1500, (b) 1800, and (c) 2100 UTC 11 Jul, and (d) 0000, (e) 0300, and (f) 0600 UTC 12 Jul 1981. Isobars of mean sea level pressure are at 1-hPa intervals. Station plots show winds (full barb = 5 m s^{-1}, half barb = 2.5 m s^{-1}), temperature, and dew point (°C). Fronts, troughs, and lee cyclone are depicted in customary fashion, outflow boundaries with small pips. Curves 1, . . . , 6 indicate the pressure ridges related to gravity waves.

timate (Koch et al. 1988) was made over the CCOPE mesonetwork, it is uncertain whether the rapid acceleration seen with simulated wave C occurred in reality.

Properties exhibited by the observed gravity waves agree in several respects with simulated disturbances A, B, and C. The general region affected by the waves and their propagation characteristics were predicted quite well (cf. Figs. 9 and 11). The average wavelength and phase speed of waves B and C are comparable to those observed during the second wave episode (~150 km). All the simulated waves first appeared near the observed wave generation region (Fig. 2b), and each simulated wave was attended by an outflow boundary.

Yet, there are important differences between the model forecasts and the analyzed observations. Most of the simulated disturbances are too strong, particularly insofar as simulated wave B is concerned (e.g., its closest counterpart in the observations was wave 3, but this

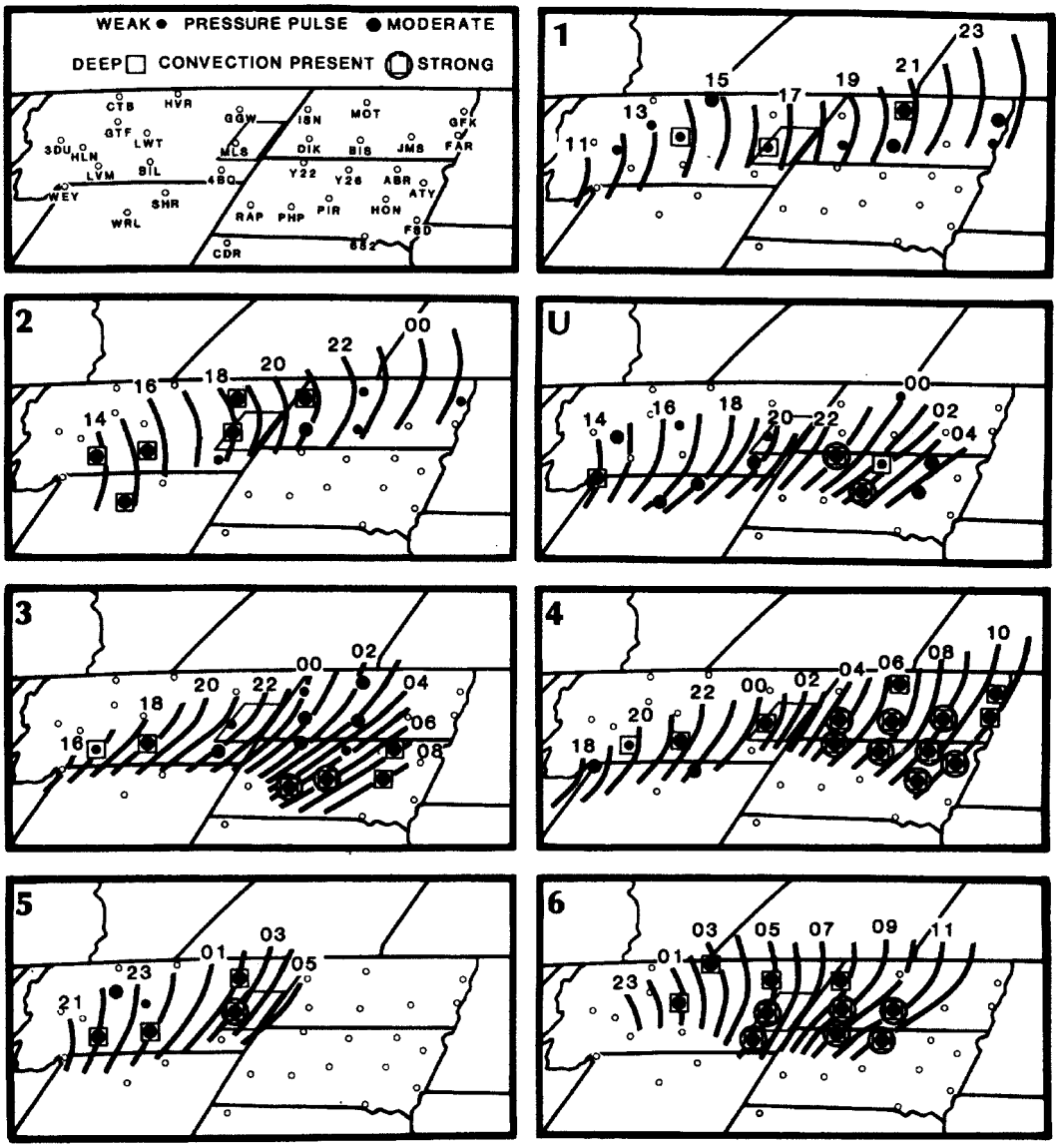

FIG. 9. Isochrones of the crests of the observed gravity waves, beginning at 1100 UTC 11 Jul and ending at 1200 UTC 12 Jul 1981. Moderate pressure pulses are defined as perturbations with amplitudes greater than 0.2 hPa. See Koch et al. (1988) for further explanation.

wave did not produce any convection until it arrived in central South Dakota). Furthermore, only about half as many gravity waves were simulated by the MM5 control run as were analyzed in the mesoscale surface data. The stationary outflow boundary observed across east-central Montana (Fig. 8c) also was not well simulated by the model. Deep convection was triggered repeatedly as one gravity wave after another passed across this stationary outflow boundary during the second wave episode, yet this was not forecast to occur in the model. In fact, this particular forecast error has implications for being able to *fully* use the model to understand the *actual* wave generation mechanism.

4) IDEALIZED MODEL SIMULATION OF WAVE C

Since wave C was generated in the lee of the Absaroka Mountains and could clearly be traced back to the wave generation region in the absence of complications arising from convection in the model, this specific wave is our focus hereafter. We first turn our attention to the idealized model experiments performed with the ARPS model, in order to understand whether simple dynamics that do not involve three-dimensional effects and geostrophic adjustment can explain the process of formation for this gravity wave.

Three-hourly displays of potential temperature, horizontal wind, and vertical motions simulated by ARPS

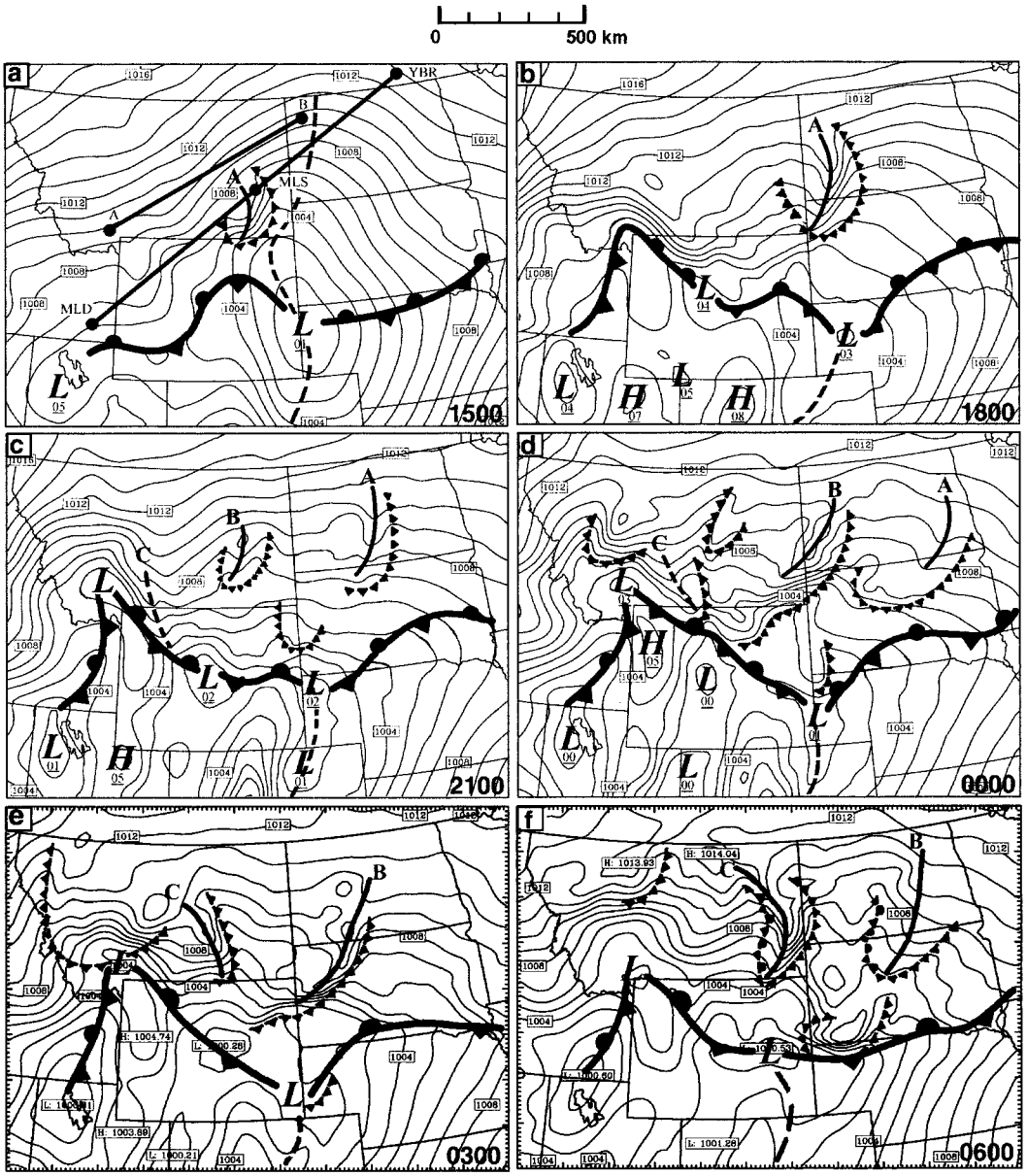

FIG. 10. As in Fig. 8 except showing control simulation forecast mean sea level pressure (contour interval 1 hPa). Curves A, B, and C indicate the location of the surface pressure ridges related to mesoscale gravity waves. Thick lines A–B and MLD–MLS–YBR depict the location of the cross sections for the control simulation and the idealized model. Note distance scale.

are shown in Fig. 15. Prior to 1500 UTC, only weak katabatic flow was present, with no indication of gravity wave activity. The nocturnal inversion begins to erode first over the mountaintop with the onset of diurnal heating (Fig. 15a). Although the downslope flow is still present at this time (note the downward perturbation in the horizontal winds in Fig. 15b), weak upslope motion has begun to appear over the eastern side of the barrier (Fig. 15c). The ARPS simulation bears strong resemblance to the sunrise state of the conceptual model presented in Fig. 1a in most respects.

With continued sensible heating, a deep planetary boundary layer (PBL) rapidly develops, reaching 5.3 km by 1800 UTC (Fig. 15d). A pronounced LCZ (Fig. 15e) and low-level updraft of 0.3 m s^{-1} (Fig. 15f) are created as westerly momentum near the mountaintop encounters the well-developed upslope flow ~75 km to its east. Completing the MPS circulation is a return current at midlevels forced by intense horizontal divergence. These features are strikingly similar to the developing MPS phase of the conceptual model (Fig. 1b).

Gravity waves are generated as the MPS updraft im-

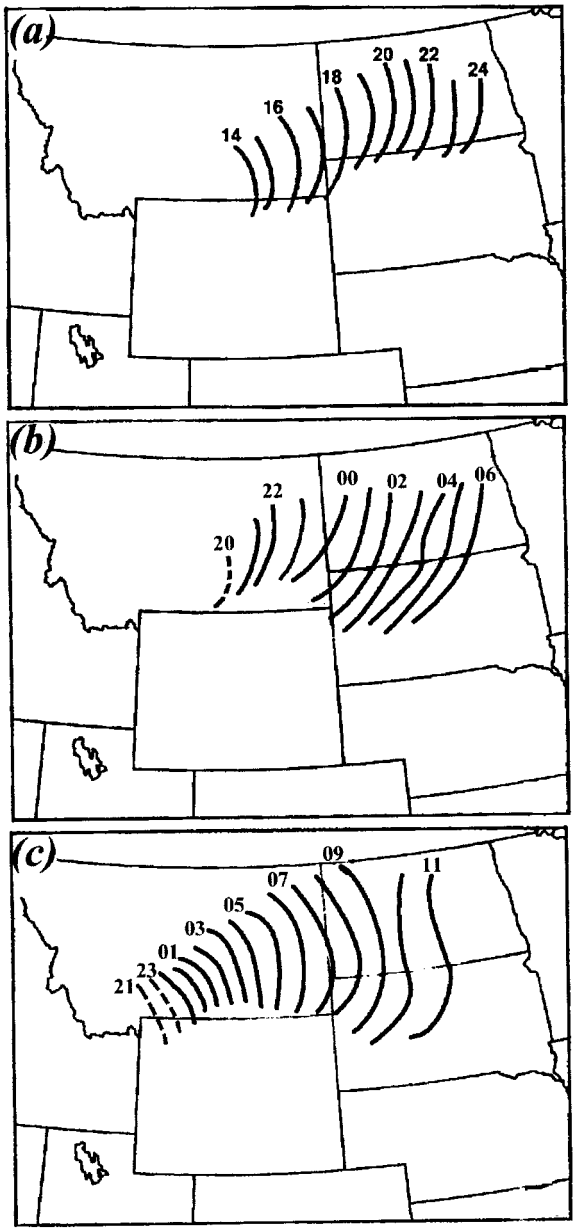

FIG. 11. Hourly isochrones (UTC) of the crests of the three waves analyzed from the control simulation: (a) wave A, (b) wave B, and (c) wave C as denoted in Fig. 10.

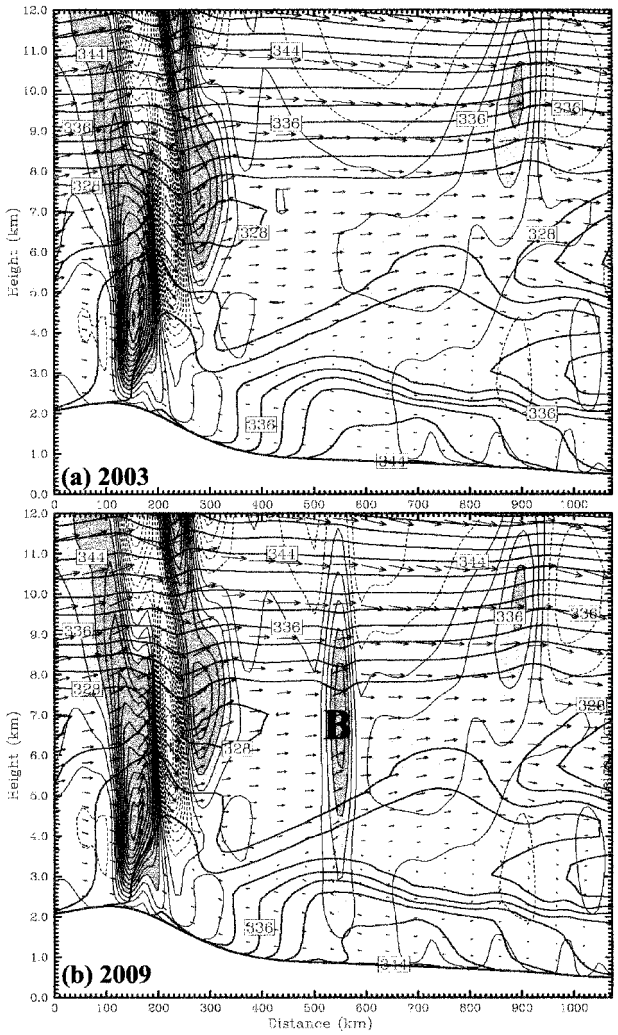

FIG. 12. Cross sections (A–B in Fig. 10a) from the control simulation of forecast potential temperature (solid lines, $\Delta = 2$ K), vertical velocity (3 cm s^{-1} intervals, with upward motions shaded), and two-dimensional wind vectors from the control circulation at (a) 2003 and (b) 2009 UTC 11 Jul 1981 showing the explosive development of wave B.

pinges upon the highly stratified layer above the deep PBL over the mountain (Fig. 15f). These mechanically forced waves, as well as the LCZ and other such features attributable to the MPS, were also seen in the MM5 control simulation (Figs. 6 and 13). No such gravity waves ever developed in the adiabatic ARPS simulation. This dispersive, upshear-tilted wave train subsequently propagated downstream with a phase speed of ~8.5 m s^{-1} to the lee of the mountain (Figs. 15g–i). Quite similar features were present in the MM5 control run before 2100 UTC (Fig. 6), though once moist convection developed, wave C (which is part of this wave train) became very difficult to discern (Fig. 14). The moist ARPS simulation (not shown) produced an LCZ rainband and several cool pools similar to those in the MM5 control run, but it soon diverged from the MM5 forecast. It is shown in section 5 that gravity waves virtually identical to those appearing in the ARPS simulation were also present in the fake-dry MM5 simulation.

In conclusion, the ARPS simulations suggest that wave C was generated by MPS updraft perturbing the stratified shear layer above the well-mixed PBL over the mountain. Use of this idealized model has allowed greater understanding of the underlying dynamics forcing gravity wave C seen in the MM5 model run without complications arising from model initial imbalances, convection, or changing background conditions. The virtually identical

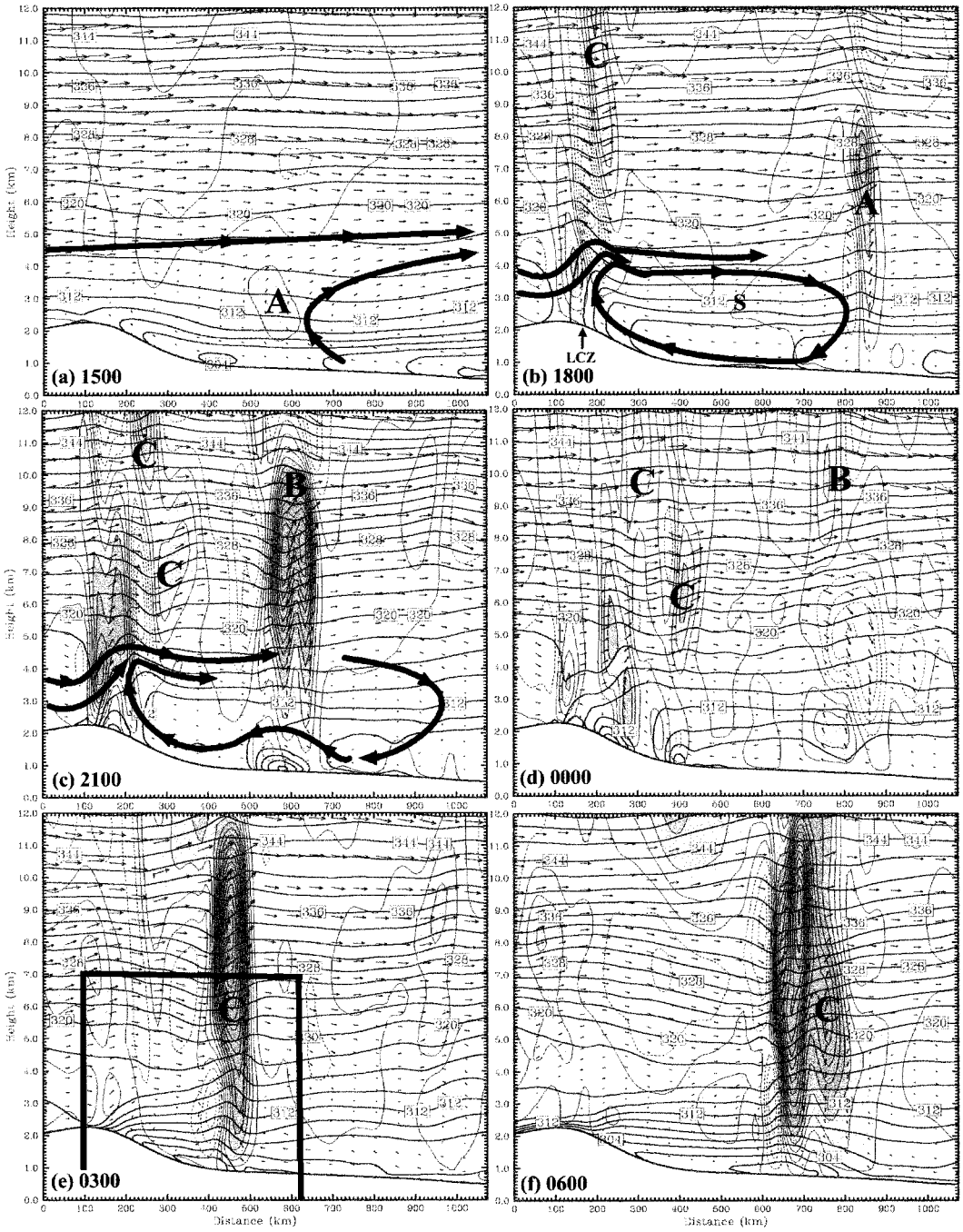

FIG. 13. As in Fig. 12 except for (a) 1500, (b) 1800, and (c) 2100 UTC 11 Jul, and (d) 0000, (e) 0300, and (f) 0600 UTC 12 Jul 1981. Labels A, B, and C indicate the locations of the gravity waves corresponding to those analyzed in Fig. 10. LCZ and general flow pattern associated with the mountain–plains solenoid (S) are also depicted at 1800 UTC. Rectangle in (e) shows the subregion displayed in Fig. 14.

nature between wave C in the MM5 simulation and that seen in the ARPS simulation shows that the forcing for this gravity wave lies in two-dimensional dry flow. In essence, the waves were forced by dynamics similar to those that govern the generation of gravity waves in a stably stratified shear layer caused by diabatic forcing beneath such a layer (e.g., Clark et al. 1986).

4. Diagnostic analysis of flow imbalance

Since both the observational study by Koch and Dorian (1988) and the numerical study by Kaplan et al. (1997) suggested that geostrophic adjustment played a pivotal role in generating the gravity waves in this event, the MM5 simulations were evaluated to determine the

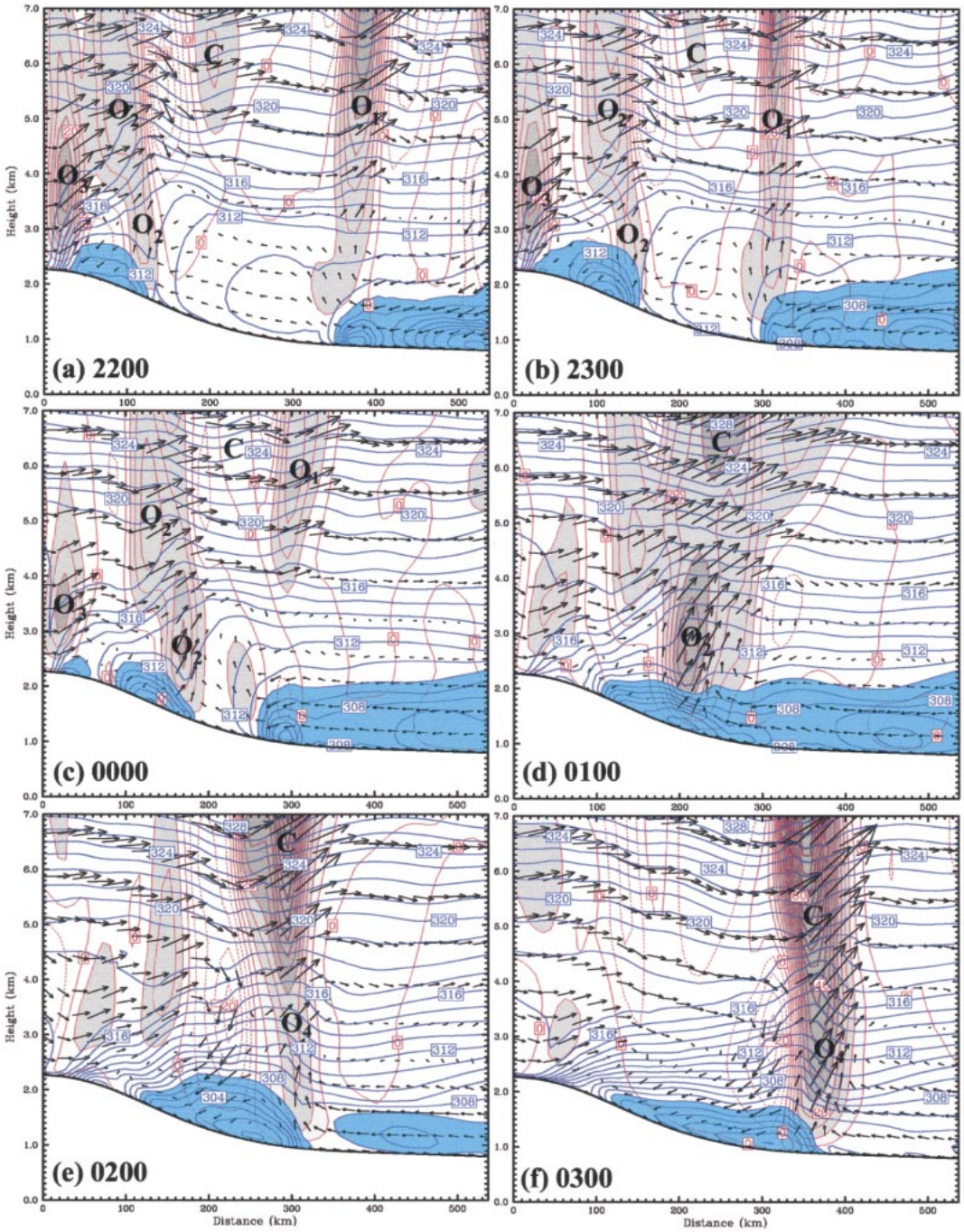

FIG. 14. As in Fig. 13 except for zoomed region depicted in Fig. 13e at (a) 2200 and (b) 2300 UTC 11 Jul, and (c) 0000, (d) 0100, (e) 0200, and (f) 0300 UTC 12 Jul 1981. Blue shading demarcates cool pools produced by evaporation of precipitation. Updrafts along outflow boundaries are numbered $O_1, \ldots, O_4$.

possibility of flow imbalance. The height field and southwesterly jet stream at 300 hPa evolved very slowly during the 9-h period ending at 0000 UTC 12 July (Fig. 16). Jet streak J2 propagated away from the trough over the Pacific Northwest and toward the broad ridge over Minnesota. This placed the wave generation region at the right entrance region of J2 during the midafternoon. Given this observation and the fact that the surface stationary frontal boundary was directly southeast of the jet (Figs. 8 and 10), then this synoptic environment is broadly consistent with the gravity wave conceptual model identified by Uccellini and Koch (1987). Therefore, the implication is that geostrophic adjustment should be considered as a wave source mechanism.

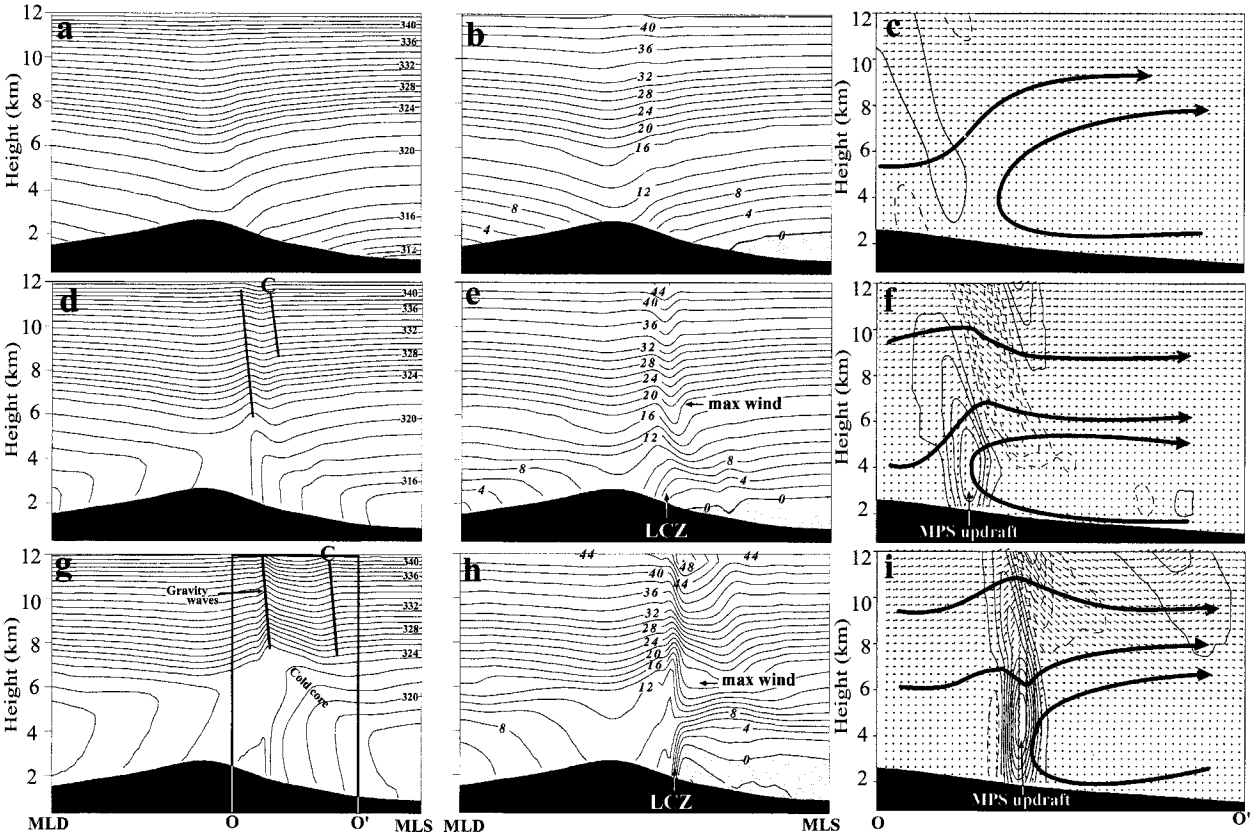

FIG. 15. Simulated fields produced by ARPS dry, two-dimensional model over identical terrain to that used in the MM5 model simulations: (a) potential temperature (1-K isentropes), (b) horizontal wind in the plane of the cross section (2 m s^{-1} intervals, negative shaded), and (c) vertical circulation (vectors) and vertical motions (3 cm s^{-1} intervals, upward solid, downward dashed). Forecast fields are shown for 1500 UTC 11 Jul in (a), (b), and (c), 1800 UTC in (d), (e), and (f), and 2100 UTC in (g), (h), and (i). Vertical motion contours in (f) and (i) are 5 and 15 cm s^{-1}, respectively. Box OO′ in (g) denotes the location of (c), (f), and (i).

Nevertheless, it is clear from the analysis of the previous section that orography must also be considered in understanding the development of the second wave episode, just as originally suggested by Koch and Dorian (1988). Since topography can have a very pronounced effect on the airflow, its role in modifying the dynamics of the upper-tropospheric jet streak as it crossed the mountain must be evaluated. The dry model simulation performed by Kaplan et al. (1997, hereafter K97) showed that J2 formed at approximately 0800 UTC in response to inertial-advective forcing accompanying the broader synoptic-scale jet stream. Their simulation further suggests that thermal wind imbalance accompanied J2 precisely over the wave generation region of southwestern Montana (Fig. 2b), and that a pronounced leftward-directed ageostrophic flow developed in the right entrance region of J2 by 1200 UTC over this same area. Since this was also the *exit* region of the geostrophic wind maximum (located back over Idaho), it appeared that the ageostrophic flow was unbalanced. This assertion was supported by computations revealing both a large Lagrangian Rossby number and residual in the nonlinear balance equation right over the wave generation region. K97 speculated that this transverse ageostrophic circulation was also responsible for generating a midlevel (~725 mb) jet over southeastern Idaho, which in turn, generated stationary mountain waves as it interacted with the Absaroka Mountains. However, the imbalance indicator fields seemed to merely reflect the appearance of these waves, rather than serving as predictors of where and when propagating gravity waves should appear.

Zhang et al. (2000) review the theory and application of various diagnostics for determining the existence of unbalanced flow, such as the nonlinear balance equation, nonquasigeostrophic vertical motions, the Lagrangian Rossby number, and fields of balanced geopotential and vertical motions derived from potential vorticity inversion techniques. They show that the residual of the nonlinear balance equation (NBE) contains sufficient information required to assess flow imbalance. Since K97 used the NBE residual and Koch and Dorian (1988) utilized the Lagrangian Rossby number, we have chosen to discuss those fields here for diagnosing the flow imbalance prior to and during the second wave episode.

The NBE residual throughout the entire domain was

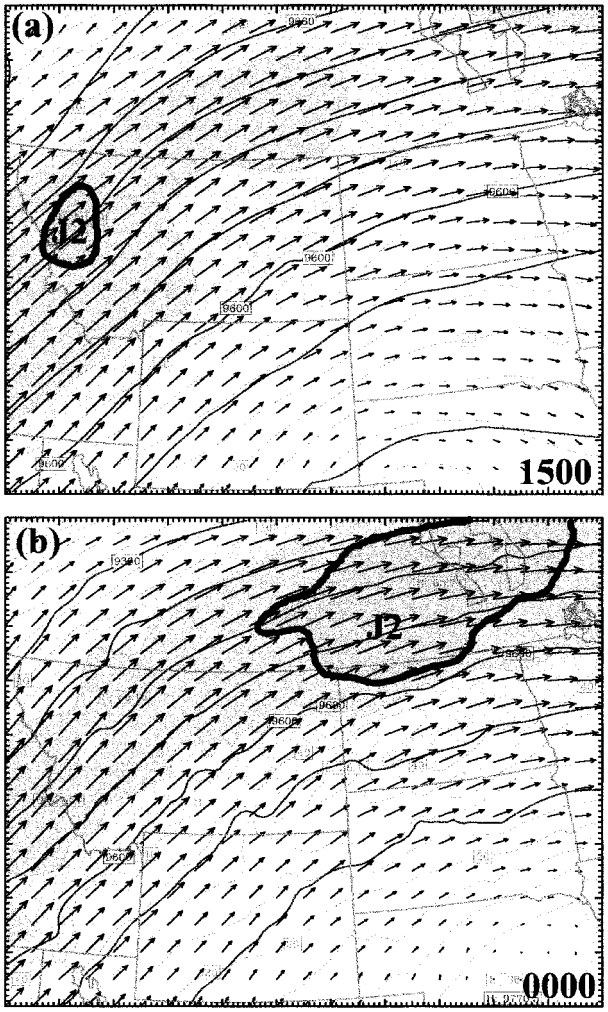

FIG. 16. Control run simulated 300-hPa geopotential heights (solid lines, 4-dam intervals), wind vectors, and isotachs (dotted, 5 m s^{-1} intervals, wind speeds >35 m s^{-1} shaded) valid at (a) 1500 UTC 11 Jul 1981 and (b) 0000 UTC 12 Jul 1981. Jetlet J2 is highlighted.

$<0.5 \times 10^{-8}$ s^{-2} before 1500 UTC (not shown); in other words, the flow was nearly balanced early in the model simulation (recall that there was no wave activity near the mountains at that time in the MM5 model simulations). Yet, K97 diagnosed strong imbalance in their model simulation at these times. There are two reasonable explanations for this discrepancy. First of all, MM5 was initialized at 1200 UTC 11 July, whereas the model that they used was initialized 12 h earlier. This meant that their model had 12 h longer to generate mesoscale circulations that might be manifested in the imbalance indicator fields. Second, a comparison of the local soundings to the model initial conditions revealed that the initial state used in the MM5 simulation more faithfully replicated the observed atmosphere at 1200 UTC than did the 12-h forecast shown by K97. In particular, the MM5 initial state showed strong stratification in the lowest 100 mb, above which reduced stability existed up to ~500 mb (5.5 km), where enhanced stability once again was found. This structure is still present in the 3-h MM5 forecast valid at 1500 UTC (Fig. 13a). By contrast, a similar cross section shown as Fig. 19d in K97 does not exhibit the strong low-level stratification and the layer of reduced stability is much thicker than observed. Both of these forecast errors would tend to amplify the magnitude of any perturbations generated by the model.

Notwithstanding this difference between the two model simulations, flow imbalance was eventually generated in the control run of the MM5 model over the Absaroka Mountains, as the NBE residual increased by an order of magnitude to $\sim 5.9 \times 10^{-8}$ s^{-2} by 1800 UTC over the wave generation region (Fig. 17b). The hourly evolution of the magnitude of the maximum NBE residual over the mountains shows a sharp increase from 1700 to 2000 UTC[1] (Fig. 18) as the MPS updraft reached its greatest strength and gravity wave C began to propagate eastward away from the mountain (Figs. 10, 13). The residual attained a very high value of $\sim 11.5 \times 10^{-8}$ s^{-2} shortly after 2000 UTC. Thereafter, the magnitude of the NBE residual over the mountains dropped significantly, though imbalances caused by convection associated with waves B and C increased (Figs. 17c,d).

The Lagrangian Rossby number field (not shown) exhibited patterns and evolution very similar to those seen in the NBE residual field. These fields merely reflect the presence of the mesoscale perturbations in the mass and momentum fields, rather than serving as effective predictors of where inertia–gravity waves will likely form. In fact, convection produced most of the perturbations beyond the region of terrain forcing (compare these fields to Fig. 10). Thus, the imbalance indicator fields in this case serve no useful predictive purpose. Yet, it is understandable why Koch and Dorian (1988) proposed that geostrophic adjustment might have generated the observed waves upstream of the CCOPE mesonetwork. Since they were forced to rely upon mainly synoptic-scale rawinsonde data, they could not resolve the spatial details in the imbalance indicator fields, nor their rapid temporal changes or actual cause.

5. Sensitivity tests

a. Fake-dry simulation

The fake-dry experiment serves a useful purpose, since the gravity waves can be studied apart from the complications arising from simulated convection in the control run, while containing considerable more complexity than in the two-dimensional ARPS simulations. Several weak gravity waves were produced in the fake-

[1] Notice that the imbalance at the model initial time caused by the static initialization procedure disappears in only 1 h and, so, has no relationship to the strong imbalance diagnosed by 1800 UTC.

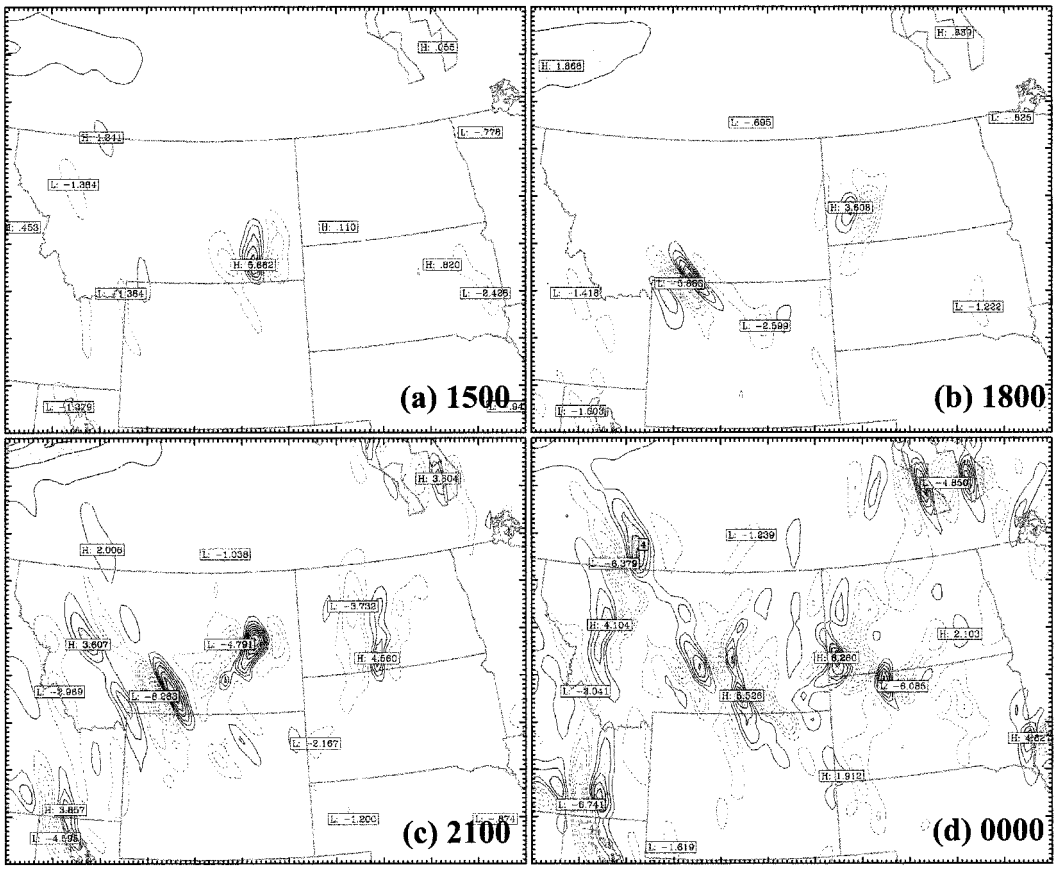

FIG. 17. NBE residual at 300 hPa from the control simulation (positive values are solid and shaded, negative are dashed, at intervals of 1×10^{-8} m s^{-2}) valid at (a) 1500, (b) 1800, and (c) 2100 UTC 11 Jul, and (d) 0000 UTC 12 Jul 1981.

dry experiment, but only wave C was pronounced and also originated as a disturbance over the Absaroka Mountains (Fig. 19). The origin, evolution, and characteristics of this gravity wave are very similar to wave C appearing in the control simulation prior to ~2000 UTC, as well as the ARPS simulation. Wave C was strongest and most persistent in the vertical motion fields above 7 km. Its 150-km horizontal wavelength (twice the distance between the ridge and trough in the isentropes) and source region (Fig. 20) are in good agreement with the waves observed in episode II by Koch et al. (1988). However, its propagation speed of ~11.1 m s^{-1} is only 60% of that observed.

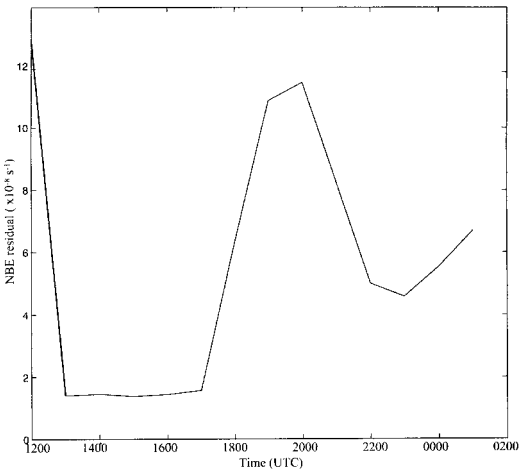

FIG. 18. Evolution of the hourly 300-hPa maximum NBE residual from 1200 UTC 11 Jul to 0000 UTC 12 Jul 1981.

The role of unbalanced dynamics in the generation of wave C can be assessed with less ambiguity than in the control run because of the absence of the complicating effects of moist convection and uncertainties arising from the merger of density currents. Comparison of the NBE residual fields at 300 hPa from the fake-dry simulation (Fig. 21) and those from the control run (Fig. 17) shows negligible difference over the mountains at 1500 and 1800 UTC, though the imbalance related to convection (wave A) is obviously absent in the fake-dry run. Magnitudes of the NBE residual and Rossby number in the fake-dry run increased more rapidly than those in the control simulation from 1500 UTC 11 July to 0000 UTC 12 July. The maximum NBE residual was almost twice that seen in the control simulation at 2000

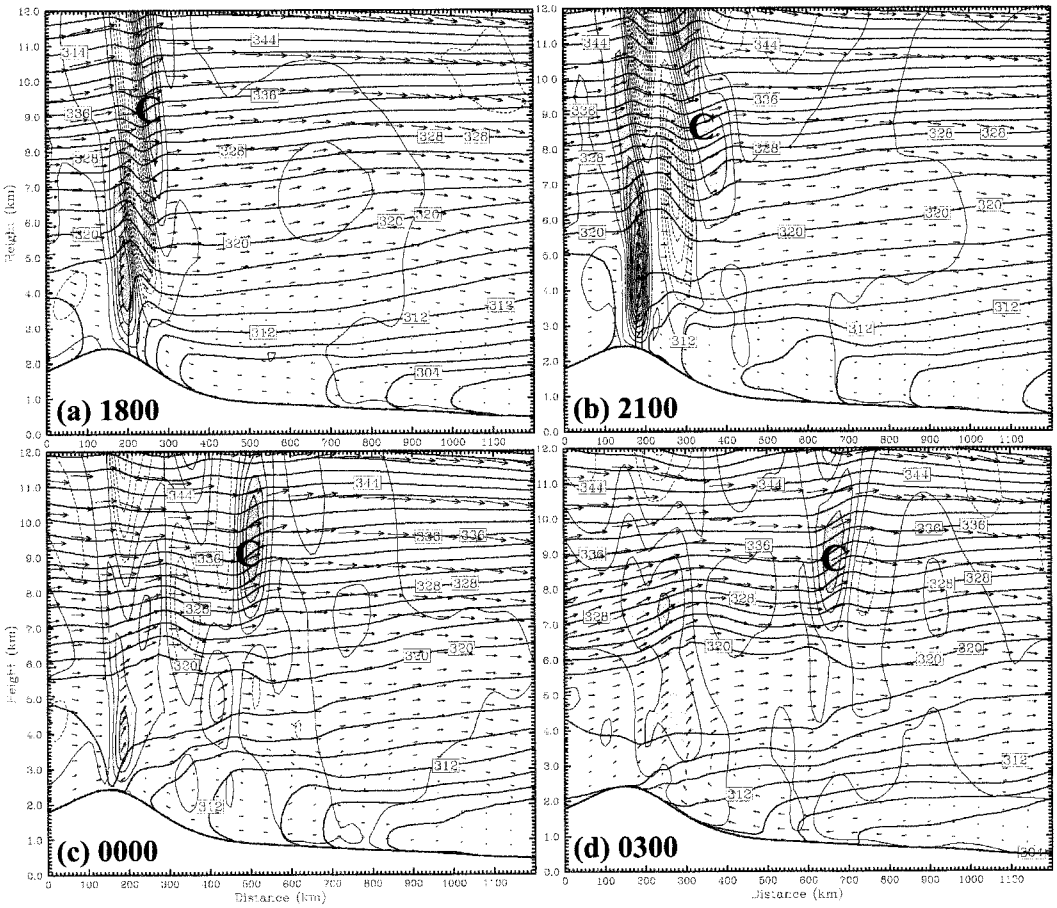

FIG. 19. As in Fig. 13 except for the fake-dry simulation valid at (a) 1800 and (b) 2100 UTC 11 Jul, and (c) 0000 and (d) 0300 UTC 12 Jul 1981 along line C–D in Fig. 20.

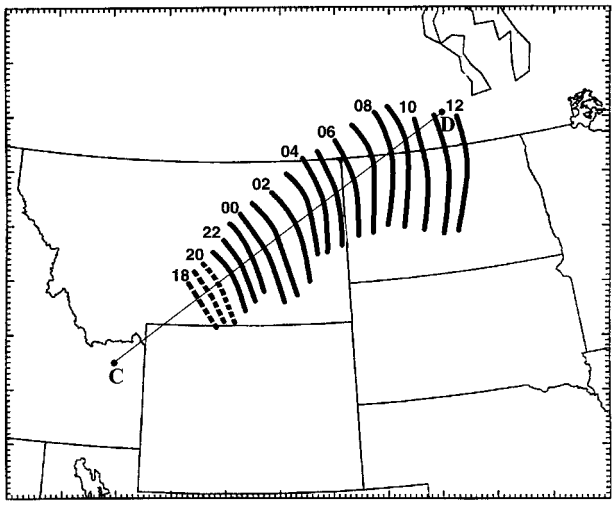

FIG. 20. Hourly isochrones of gravity wave C analyzed from the 300-hPa vertical motion field in the fake-dry simulation. Line C–D indicates the location of the cross sections shown for the fake-dry and adiabatic simulations.

UTC, and continued to intensify until after 2100 UTC, when the wave began to propagate downwind of the mountain. It appears that in the absence of cool downdrafts by moist convection, the imbalance related to the mass perturbation associated with the strong sensible heating was larger.

The Laplacian of the geopotential height was found to be the dominant factor contributing to the large residual of the NBE in both the control simulation and the fake-dry run. In fact, at 2000 UTC when the NBE residual was the strongest, the Laplacian term ($\nabla^2\phi$) was more than 10 times larger than the other terms in the NBE. The temporal behavior of the Laplacian term correlates very well with the sensible heating near the surface (Fig. 22). Thus, it may be concluded that differential sensible heating between the mountains and the atmosphere was crucial for generating the large imbalance. Additional evidence is provided by the results of the adiabatic and no-terrain simulations discussed next.

b. Adiabatic simulation

An adiabatic simulation disallowing sensible heating was also performed to further understand the separate

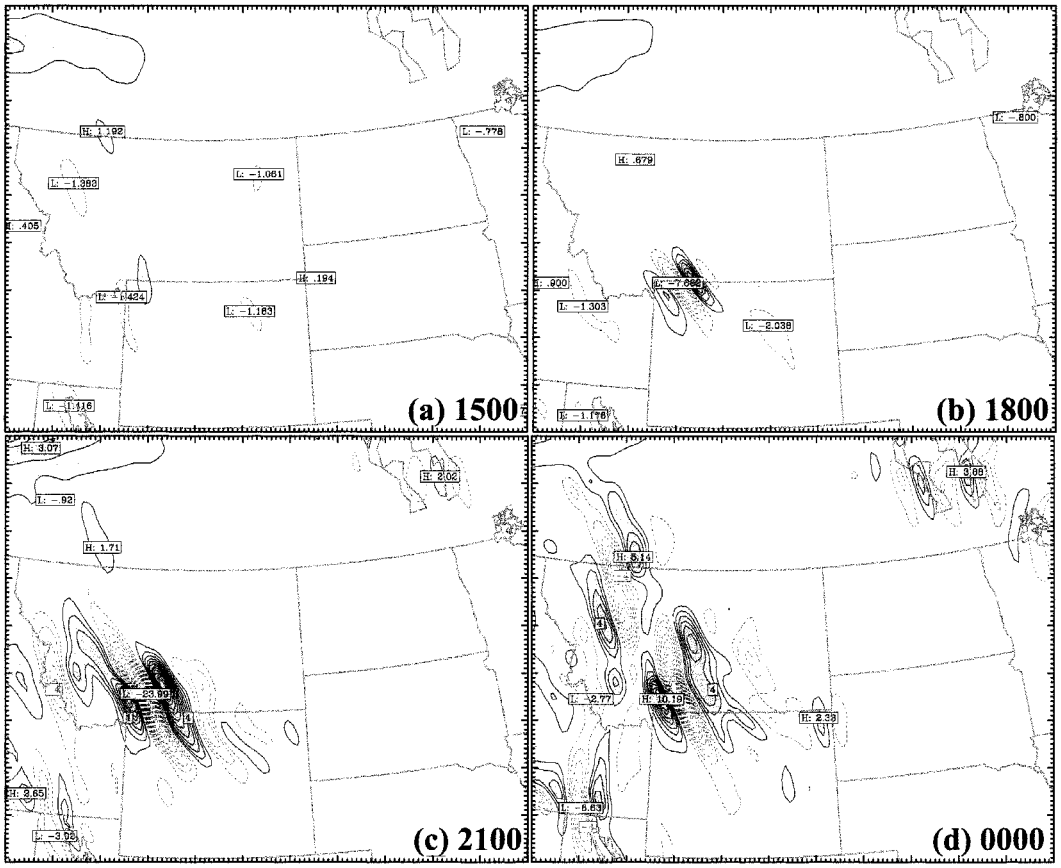

FIG. 21. As in Fig. 17 except for the fake-dry simulation.

contributions of differential sensible heating (the MPS) and dynamic forcing by the underlying topography in generating the gravity waves and associated imbalance. Propagating gravity waves never developed in this simulation (not shown) and wave activity above the Absaroka Mountains was much weaker than in the control and fake-dry simulations. Not surprisingly, the NBE residual grew very slowly to a magnitude of only 2.5 $\times 10^{-8}$ s^{-2} during the first several hours and suffered from being incoherent thereafter.

c. *Flat-terrain simulation*

Without the mountainous terrain, no gravity waves were excited in southwestern Montana or northwestern Wyoming. Likewise, the large imbalance indicated by the NBE residual over the Absaroka Mountains in the control and fake-dry simulations never appeared in this simulation (though there were many small regions of imbalance related to convection). The no-terrain and adiabatic simulations together provide convincing support for our assertion that *heating over the complex terrain of the Absaroka Mountains was a necessary factor for creating the imbalance and generating gravity waves.*

6. Shear instability and wave ducting

As shown in Fig. 23, a wave critical level existed at the 4.5–5.0-km level coincidentally with Richardson number Ri < 0.115 in both the control and fake-dry simulations slightly to the east of the mountain peak at 2100 UTC. Thus, the necessary conditions for shear instability and wave overreflection were met in both simulations at the time that wave C was quite pronounced and starting to propagate eastward. Similarly, Koch and Dorian (1988) and Koch et al. (1993) showed from shear and linear stability analysis that the waves over the CCOPE mesonetwork could efficiently extract energy from the mean flow near several closely spaced critical levels with low Richardson number in the 3.5–5.5-km layer. The CCOPE mesonetwork is in eastern Montana, which is at $\sim x = 800$ km in both Fig. 23a and Fig. 23b. Notice that a second region of low Ri at a critical level is found at this location. However, the conditions for shear instability were not met in either simulation in between the two regions of low Ri over CCOPE and farther west over the mountains. Thus, this mechanism could not have provided a sustained source of energy for the waves all the way from their point of origin to eastern Montana.

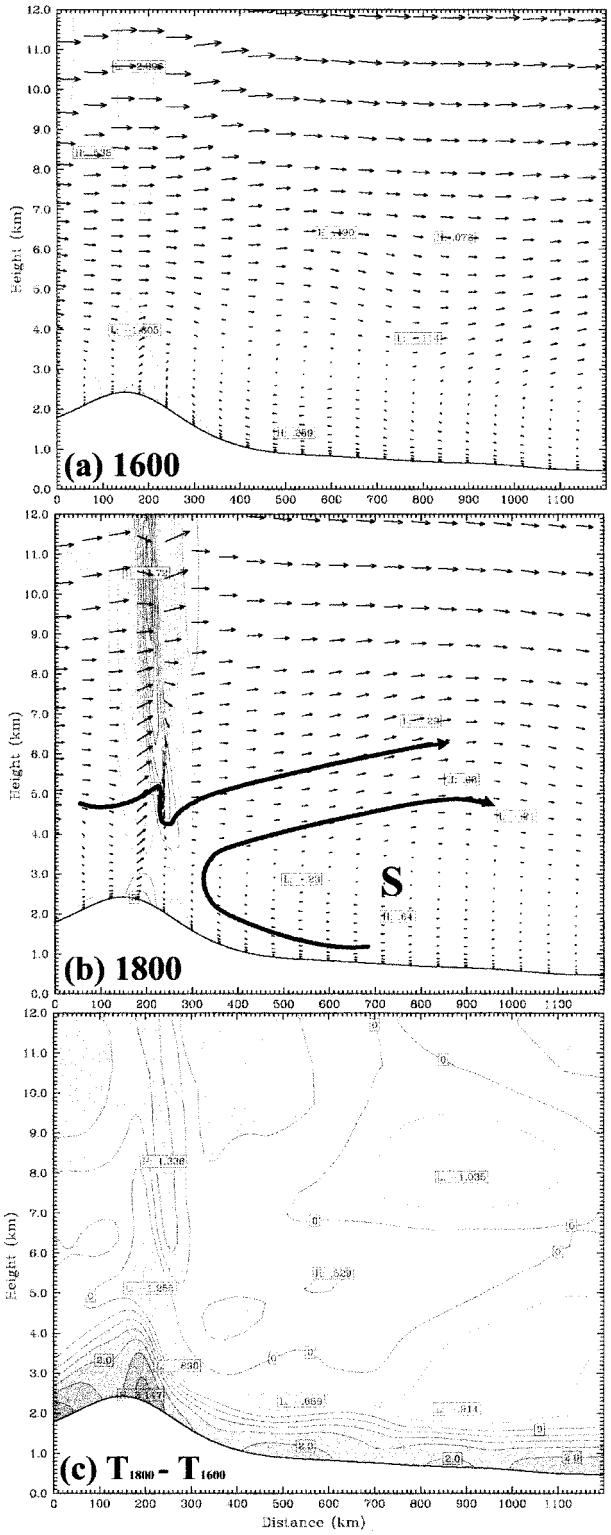

FIG. 22. Cross sections of Laplacian of the geopotential heights (positive values are solid and shaded, negative are dashed at intervals of 2×10^{-8} s^{-2}) and wind vectors (location shown in Fig. 20) from the fake-dry run at (a) 1600 and (b) 1800 UTC. The S denotes center of mountain–plains solenoid. (c) Temperature change in the fake-dry run from 1600 to 1800 UTC along cross-section line C–D (warming denoted by solid lines, cooling by dotted lines, every 0.5°C).

Wave C never appeared in the mean sea level pressure fields in the fake-dry simulation. This suggests that wave ducting alone was not sufficient to contain the wave energy in the low levels and that moist convective processes were necessary to maintain and amplify the waves. Although it is true that diurnal heating destroyed the low-level stratification over the mountains, an elevated layer of static stability persisted in the 1.3–3.0-km layer to the east of the base of the mountains (Fig. 23a), which is particularly evident in the fake-dry run. For a stable layer to act as an efficient wave duct, its depth D_1 must be (Lindzen and Tung 1976; Lin and Wang 1996)

$$D_1 = \frac{\pi}{2}\frac{(C - U_1)}{N_1}.$$

For the fake-dry run, the wave phase speed $C = 11.1$ m s^{-1}, the Brunt–Väisälä frequency in the stable layer $N_1 = \sqrt{0.000\ 15\ s^{-2}}$, and the mean wind $U_1 = 4$ m s^{-1}, giving $D_1 = 1.9$ km. This depth is quite close to the simulated depth of 1.7 km, suggesting that a wave duct was present well east of the mountains. This is consistent with the calculations performed from the observations over the CCOPE mesonetwork by Koch and Dorian (1988). We conclude that the reason simulated wave C in the fake-dry run was perceptible only in the middle-to-upper troposphere and not at the surface is that the wave duct was not felt by this gravity wave until it had propagated more than one to two horizontal wavelengths to the east of the mountains. The highly variable ducting properties of the atmosphere between the data-sparse wave generation region in southwestern Montana and the data-rich CCOPE mesonetwork in eastern Montana could not be determined from the observations available to Koch and Dorian (1988).

Linear stability analyses and multiple Doppler radar pressure retrievals performed by Koch et al. (1993) both suggested a ducted gravity wave confined between the ground and the first nodal surface at an altitude of 2.0–3.3 km above the ground (the lower estimate being based on linear theory). This wave structure is clearly at odds with the fake-dry MM5 and ARPS simulations showing nearly all of the wave energy confined to the stable layer above the well-mixed PBL. This discrepancy between model and observations is easily explained upon considering that the wave generation mechanism in the model simulations was mechanical forcing by the MPS updraft. Hence, these model simulations do not support the assumption of a free wave that underlies linear stability theory. Furthermore, the Doppler radar analysis was performed over extreme eastern Montana at 0100 UTC 12 July after convection had already appeared; thus, it was done over a region of pronounced wave ducting and is not representative of the area in which the gravity waves were generated.

In summary, this set of model-based analyses further supports the argument that wave-CISK was responsible

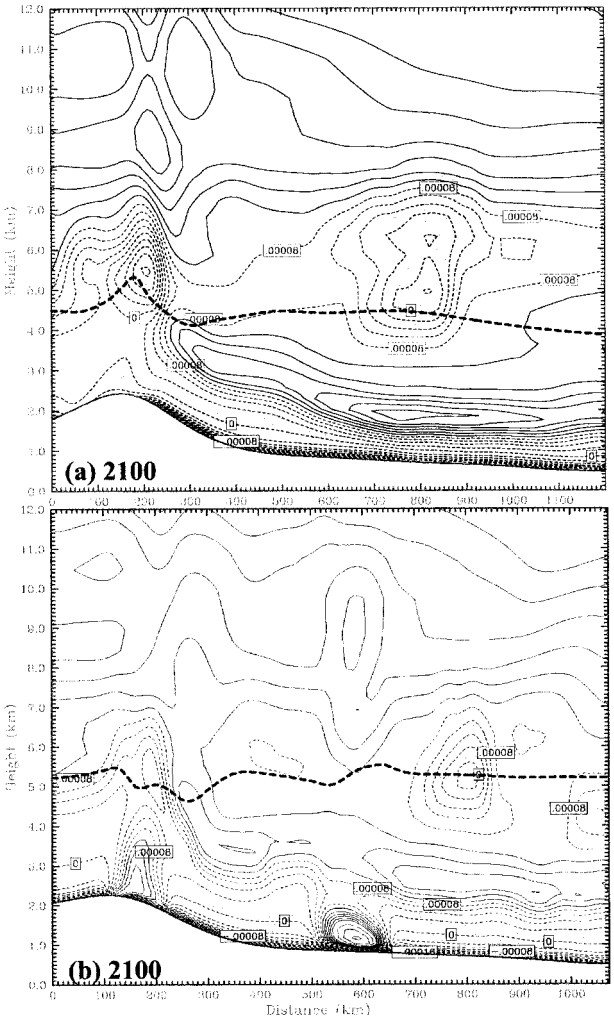

FIG. 23. Cross sections of square of moist Brunt–Väisälä frequency (N^2, intervals of 0.000 02 s^{-2}, thin dashed lines indicate $N^2 < 0.0008$ s^{-2}) valid at 2100 UTC 11 Jul 1981. The area shaded indicates Richardson number Ri < 0.25 and the thick dashed line shows the wave critical level. (a) Cross section along line C–D in Fig. 20 for fake-dry run assuming a wave speed of 11.1 m s^{-1} and (b) cross section along line A–B in Fig. 2a for the control simulation assuming a wave speed of 15.0 m s^{-1}.

for maintaining propagating gravity waves that were generated by other processes (MPS forcing and outflow boundary interactions). Neither geostrophic adjustment, nor shearing instability, nor wave ducting played important dynamical roles in this event according to the simulations. Unfortunately, the crucial observations needed to confirm the validity of these simulations were not available in the wave generation region itself; rather, the detailed observations were only taken over the CCOPE mesonetwork shown in Fig. 2a. This kind of data problem is not unique to the CCOPE event, for it has hampered the ability of all published studies of mesoscale gravity waves to make definitive conclusions, often to a greater degree than in the present case.

7. Summary and discussion

A gravity wave event that occurred during CCOPE has been investigated with the nonhydrostatic PSU–NCAR MM5 version 2 model. Detailed observations from surface mesonetwork data and multiple Doppler radar analysis, as well as the results from linear stability analysis and other mesoscale model investigations of this event published elsewhere, have afforded an unprecedented opportunity for making careful comparisons with the model results discussed here.

Multiple source mechanisms for the simulated gravity waves were identified in the model. Wave A appeared too early in the integration of the model to give much confidence as to its realism, though it shared some characteristics with the observations. Simulated wave B was a wave-CISK mode that developed explosively in an elevated layer of instability west of the CCOPE region. Precipitation associated with this wave created a cool pool that spread westward and merged with another cool pool that was sliding down the lee slopes of the Absaroka Mountains in western Montana. As the two outflow boundaries collided, strong convection was triggered right beneath a weakening gravity wave C that had been generated earlier by the updraft over the mountaintop associated with a pronounced mountain–plains solenoid circulation. Wave C was reinvigorated and subsequently evolved into a strong long-lasting bore wave that propagated across the CCOPE region and the Dakotas. The general region affected by the waves, their source region, their propagation characteristics, and wavelengths were all in good agreement with the detailed mesoscale analyses performed by Koch et al. (1988). However, the model produced too few and generally too strong waves, and the associated convection predicted by the model lacked realism in certain respects.

Since wave C was generated in the lee of the Absaroka Mountains and could be isolated apart from the problems related to moist convection and initialization concerns, detailed analysis was performed of its genesis and maintenance mechanisms. A dry, two-dimensional model was used to better understand its basic dynamics. This model produced a virtually identical gravity wave to that in the MM5 control and fake-dry simulations. Mechanical forcing generated this upshear-tilted wave as the MPS updraft perturbed the stratified shear layer above the well-mixed PBL resulting from strong sensible heating over the mountains.

The role of flow imbalance (geostrophic adjustment) in the wave generation was investigated with the MM5 model because Koch and Dorian (1988) and Kaplan et al. (1997) had previously suggested its importance in this event. The nonlinear balance equation and Rossby number fields both indicated that large imbalance appeared simultaneously with the development of the gravity waves forced by the impinging MPS. The Laplacian of the geopotential height was by far the dom-

inant term causing the large residual in the nonlinear balance equation. This term became large because of the height perturbation caused first by the upward-propagating wave in the stable layer above the mountain, and later by wave C that propagated eastward out of this wave field. It was not possible to distinguish cause from effect, since the imbalance occurred simultaneously with the waves, though the results from the two-dimensional model cast considerable doubt on the importance of geostrophic adjustment in the wave generation process.

Sensible heating over the high topography in western Montana and northwestern Wyoming was essential in creating the gravity waves. No waves were present in either the adiabatic simulation, which disallowed surface sensible heating, or the flat-terrain simulation, because the requisite MPS forcing could not occur. In the fake-dry run that disallowed diabatic effects owing to precipitation, but allowed for sensible heating over the complex terrain, gravity waves were generated in the middle–upper troposphere. However, the signal of the gravity wave at the surface was much weaker than in the control simulation because of the absence of strong wave ducting near the surface immediately downstream of the mountains and any wave-CISK mechanism. A wave duct was present in the MM5 model forecast fields and the rawinsonde observations farther downstream over the CCOPE mesonetwork (Koch and Dorian 1988), and also as indicated in the wave perturbation fields predicted by linear stability theory and derived from Doppler radar pressure retrievals (Koch et al. 1993). However, this region was apparently too far displaced ($>$200 km) from the wave generation region in southwestern Montana for the waves to be able to ''tap'' this duct to preserve themselves in the presence of energy dispersion.

Mesoscale analysis of the CCOPE observations suggests that instead of the merger of two opposing gravity currents (cool pools) generating one pronounced gravity wave (or bore), thunderstorms were repeatedly generated as one gravity wave after another passed across a *stationary* outflow boundary. The MM5 model did not simulate well this boundary nor this observed process. Unfortunately, crucial observations over the wave generation region upstream of the CCOPE mesonetwork needed to confirm the model results do not exist.

This study demonstrates a continuing problem with all published studies of propagating mesoscale gravity waves—detailed observations of the actual wave generation process are missing. A focused field experiment involving in situ aircraft, remote sensing systems, and other special data is needed to reconcile detailed but questionable mesoscale model simulations indicating the dominance of wave-CISK modes. Our results also point to the limitations of attempting to merely use unbalanced flow indicator fields to attempt to ''prove'' that geostrophic adjustment causes the observed gravity waves, at least when complex topography and moist convection are present. In addition, the sensitivity of mesoscale model simulations of gravity waves to even modest errors in forecasts of precipitating convection remains a grand challenge.

Acknowledgments. We wish to thank Chris Davis, Yi Jin, and Yihua Wu for their constructive comments. Lisa Gray, Robert Stonefield, and Kevin Laws provided assistance with graphics. We also are appreciative of the free software for analysis of the MM5 output provided by Mark Stoelinga. This research was funded under NSF Grant ATM-9700626. The simulations were performed on the Cray T916 at the North Carolina Supercomputing Center and on the Cray machines at the National Center for Atmospheric Research.

REFERENCES

Banta, R. M., 1984: Daytime boundary-layer evolution over mountainous terrain. Part I: Observations of the dry circulations. *Mon. Wea. Rev.,* **112,** 340–356.

——, 1990: The role of mountain flows in making clouds. *Atmospheric Processes over Complex Terrain, Meteor. Monogr.,* No. 45, Amer. Meteor. Soc., 229–283.

Bossert, J. E., and W. R. Cotton, 1994: Regional-scale flows in mountainous terrain. Part II: Simplified numerical experiments. *Mon. Wea. Rev.,* **122,** 1472–1489.

Clark, T. L., T. Hauf, and J. P. Kuettner, 1986: Convectively forced internal gravity waves: Results from two-dimensional numerical experiments. *Quart. J. Roy. Meteor. Soc.,* **112,** 899–925.

Dudhia, J., 1993: A nonhydrostatic version of the Penn State–NCAR Mesoscale Model: Validation tests and simulation of an Atlantic cyclone and cold front. *Mon. Wea. Rev.,* **121,** 1493–1513.

Fovell, R. G., D. R. Durran, and J. R. Holton, 1992: Numerical simulations of convectively generated gravity waves in the atmosphere. *J. Atmos. Sci.,* **49,** 1427–1442.

Grell, G. A., J. Dudhia, and D. S. Stauffer, 1995: A description of the fifth-generation Penn State/NCAR Mesoscale Model (MM5). NCAR Tech. Note, NCAR/TN-398 + STR, 122 pp.

Haase, S. P., and R. K. Smith, 1989: The numerical simulation of atmospheric gravity currents. Part II: Environments with stable layers. *Geophys. Astrophys. Fluid Dyn.,* **46,** 35–51.

Jin, Y., S. E. Koch, Y.-L. Lin, F. M. Ralph, and C. Chen, 1996: Numerical simulations of an observed gravity current and gravity waves in an environment characterized by complex stratification and shear. *J. Atmos. Sci.,* **53,** 3570–3588.

Kaplan, M. L., S. E. Koch, Y.-L. Lin, and R. Weglarz, 1997: Numerical simulations of a gravity wave event over CCOPE. Part I: The role of geostrophic adjustment in mesoscale jetlet formation. *Mon. Wea. Rev.,* **125,** 1185–1211.

Karyampudi, V. M., S. E. Koch, J. W. Rottman, and M. L. Kaplan, 1995: The influence of the Rocky Mountains in the 13–14 April 1986 severe weather outbreak. Part II: Evolution of an internal bore and its role in triggering a squall line. *Mon. Wea. Rev.,* **123,** 1423–1446.

Koch, S. E., and P. B. Dorian, 1988: A mesoscale gravity wave event observed during CCOPE. Part III: Wave environment and probable source mechanisms. *Mon. Wea. Rev.,* **116,** 2570–2592.

——, and R. E. Golus, 1988: A mesoscale gravity wave event observed during CCOPE. Part I: Multi-scale statistical analysis of wave characteristics. *Mon. Wea. Rev.,* **116,** 2527–2544.

——, M. desJardins, and P. J. Kocin, 1983: An interactive Barnes objective map analysis scheme for use with satellite and conventional data. *J. Climate Appl. Meteor.,* **22,** 1487–1503.

——, R. E. Golus, and P. B. Dorian, 1988: A mesoscale gravity wave event observed during CCOPE. Part II: Interactions between

mesoscale convective systems and the antecedent waves. *Mon. Wea. Rev.*, **116,** 2545–2569.

——, P. B. Dorian, R. Ferrare, S. H. Melfi, W. C. Skillman, and D. Whiteman, 1991: Structure of an internal bore and dissipating gravity current as revealed by Raman lidar. *Mon. Wea. Rev.*, **119,** 857–887.

——, F. Einaudi, P. B. Dorian, S. Lang, and G. H. Heymsfield, 1993: A mesoscale gravity wave event observed during CCOPE. Part IV: Stability analysis and Doppler-derived wave vertical structure. *Mon. Wea. Rev.*, **121,** 2483–2510.

Lin, Y.-L., 1987: Two-dimensional response of a stably stratified shear flow to diabatic heating. *J. Atmos. Sci.*, **44,** 1375–1393.

——, 1994: Airflow over mesoscale heat sources. Part I: Responses in a uniform flow. *Proc. Natl. Sci. Counc. Repub. China*, **18A,** 1–32.

——, and T.-A. Wang, 1996: Flow regimes and transient dynamics of two-dimensional stratified flow over an isolated mountain ridge. *J. Atmos. Sci.*, **53,** 139–158.

Lindzen, R. S., and K. K. Tung, 1976: Banded convective activity and ducted gravity waves. *Mon. Wea. Rev.*, **104,** 1602–1617.

Locatelli, J. D., M. T. Stoelinga, P. V. Hobbs, and J. Johnson, 1998: Structure and evolution of an undular bore on the high plains and its effects on migrating birds. *Bull. Amer. Meteor. Soc.*, **79,** 1043–1060.

Lott, F., 1997: The transient emission of propagating waves by a stably stratified shear layer. *Quart. J. Roy. Meteor. Soc.*, **123,** 1603–1619.

Maddox, R. A., D. J. Perkey, and J. M. Fritsch, 1981: Evolution of upper tropospheric features during the development of a mesoscale convective complex. *J. Atmos. Sci.*, **38,** 1664–1674.

May, P. T., and J. M. Wilczak, 1993: Diurnal and seasonal variations of boundary-layer structure observed with a radar wind profiler and RASS. *Mon. Wea. Rev.*, **121,** 673–682.

Moeng, C.-H., and J. C. Wyngaard, 1988: Spectral analysis of large-eddy simulations of the convective boundary layer. *J. Atmos. Sci.*, **45,** 3573–3587.

Raymond, D. J., 1972: Calculation of airflow over an arbitrary ridge including diabatic heating and cooling. *J. Atmos. Sci.*, **29,** 837–843.

——, 1975: A model for predicting the movement of continuously propagating convective storms. *J. Atmos. Sci.*, **32,** 1308–1317.

——, 1984: A wave-CISK model of squall lines. *J. Atmos. Sci.*, **41,** 1946–1958.

Smith, R. B., 1979: The influence of mountains on the atmosphere. *Advances in Geophysics*, Vol. 21, Academic Press, 87–230.

Smith, R. K., 1988: Travelling waves and bores in the lower atmosphere: The ''morning glory'' and related phenomena. *Earth-Sci. Rev.*, **25,** 267–290.

Toth, J. J., and R. H. Johnson, 1985: Summer surface flow characteristics over northeast Colorado. *Mon. Wea. Rev.*, **113,** 1458–1469.

Tripoli, G. J., and W. R. Cotton, 1989a: Numerical study of an observed orogenic mesoscale convective system. Part I: Simulated genesis and comparison with observations. *Mon. Wea. Rev.*, **117,** 273–304.

——, and ——, 1989b: Numerical study of an observed orogenic mesoscale convective system. Part II: Analysis of governing dynamics. *Mon. Wea. Rev.*, **117,** 305–328.

Tyson, P. D., and R. A. Preston-Whyte, 1972: Observations of regional topographically-induced wind systems in Natal. *J. Appl. Meteor.*, **11,** 643–650.

Uccellini, L. W., and S. E. Koch, 1987: The synoptic setting and possible energy sources for mesoscale wave disturbances. *Mon. Wea. Rev.*, **115,** 721–729.

Wolyn, P. G., and T. B. McKee, 1994: The mountain–plains solenoid east of a 2-km high north–south barrier. *Mon. Wea. Rev.*, **122,** 1490–1508.

Xue, M. K., K. K. Droegemeier, V. Wong, A. Shapiro, and K. Brewster, 1995: ARPS 4.0 user's guide. CAPS, 380 pp. [Available from Center for Analysis and Prediction of Storms, University of Oklahoma, Norman, OK 73069.]

Zhang, F., and S. E. Koch, 2000: Numerical simulations of a gravity wave event over CCOPE. Part II: Waves generated by an orographic density current. *Mon. Wea. Rev.*, **128,** 2777–2796.

——, ——, C. A. Davis, and M. L. Kaplan, 2000: A survey of unbalanced flow diagnostics and their application. *Adv. Atmos. Sci.*, **17,** 1–19.